Crustal Lg attenuation within the North China Craton and its surrounding regions

Lian-Feng Zhao,[1,2] Xiao-Bi Xie,[2] Wei-Min Wang,[3] Jin-Hai Zhang[1] and Zhen-Xing Yao[1]

[1]*Key Laboratory of the Earth's Deep Interior, Institute of Geology and Geophysics, Chinese Academy of Sciences, Beijing, China.*
E-mail: zhaolf@mail.iggcas.ac.cn
[2]*Institute of Geophysics and Planetary Physics, University of California, Santa Cruz, CA 95064, USA*
[3]*Key Laboratory of Continental Collision and Plateau Uplift, Institute of Tibetan Plateau Research, Chinese Academy of Sciences, Beijing, China*

SUMMARY

We report on a broad-band high-resolution attenuation model for the North China Craton and surrounding regions based on regional *Lg*-wave data. Vertical broad-band waveforms recorded at 39 stations from 176 crustal earthquakes are collected to extract the *Lg*-wave amplitude spectra between 0.05 and 10.0 Hz. We use the dual-station method to generate a preliminary Q_{Lg} model and use it as the initial model. Then, we combine the dual- and single-station data together to jointly invert the Q_{Lg} distribution and *Lg* source excitation functions. These inversions are conducted independently at individual frequencies without using any *a priori* assumption about the frequency dependences in Q_{Lg} and source terms. The maximum spatial resolution is approximately $1° \times 1°$ in well-covered areas for frequencies between 0.05 and 2.0 Hz. The Q_{Lg} image is then used to determine the relationship between the attenuation and different geological structures. Results show an average Q_0 (1 Hz Q_{Lg}) of 374 for the entire North China Craton with an increasing trend from east to west. Average Q_0 values are 337, 361 and 421 for the east, central and west blocks, respectively. For the surrounding regions, the Eastern Tibetan plateau has a very low Q_0 of 188, while the Northeast China Plate and the Tianshan–Xingmeng fold belts are characterized by high Q_0 values of 506 and 424, respectively. We also investigate regional variations of the *Lg* attenuation in low-frequency band between 0.2 and 1.0 Hz.

Key words: Body waves; Seismic attenuation; Seismic tomography; Crustal structure.

GJI Seismology

1 INTRODUCTION

The North China Craton (NCC) is a continental craton located in the middle of eastern China (refer to I in Fig. 1a). It consists of two major Archaean (older than 2.5 Ga) continental nuclei surrounded by Palaeoproterozoic (older than 1.8 Ga) orogenic belts. The first nucleus is approximately within the boundary of the Ordos basin, and the second one is beneath the Bohai Bay basin and its surrounding areas (e.g. Zhao *et al.* 2001, 2003).

Based on the occurrence of Early Palaeozoic diamondiferous kimberlites on the eastern NCC (e.g. Boyd 1989; Rudnick & Niblade 1999), the Archean or Proterozoic lithosphere mantle should be approximately 200 km thick. However, both geophysical data and studies on mantle xenoliths obtained from Cenozoic basalts indicated that the present lithosphere is much thinner (60–120 km; e.g. Menzies & Xu 1998; Zhao 2004; Chen *et al.* 2006; Lu *et al.* 2006; Menzies *et al.* 2007; Zhao & Zheng 2007; Santosh *et al.* 2008). These findings suggest that the subcontinental lithospheric

mantle underwent extensive thinning between the Ordovician and Cenozoic, and there has been significant removal of the continental lithospheric mantle since the Palaeozoic (Menzies *et al.* 1993; Griffin *et al.* 1998; Xu 2001).

The spatial–temporal variations and the geodynamics of the NCC removal have attracted much attention among geoscientists (e.g. Chen *et al.* 2003; Gao *et al.* 2004; An & Shi 2006; Wu *et al.* 2006; Ji *et al.* 2007; Xu 2007). Several models have been proposed to explain the causes and tectonic mechanisms of the Late Mesozoic to Cenozoic tectonic activities. These models can be grouped as a delaminating model and a convective downwelling model (Bird 1979; Houseman *et al.* 1981; Doin *et al.* 1997; Griffin *et al.* 1998; Wu *et al.* 2005; Deng *et al.* 2007; Menzies *et al.* 2007). Although there are still controversies regarding how the lithospheric removal happened, most researchers agree that any acceptable model should be accompanied by magma intrusion. Such intrusion results in material exchange between crust and upper mantle, and changed the components and structures of the crust. Investigating the seismic
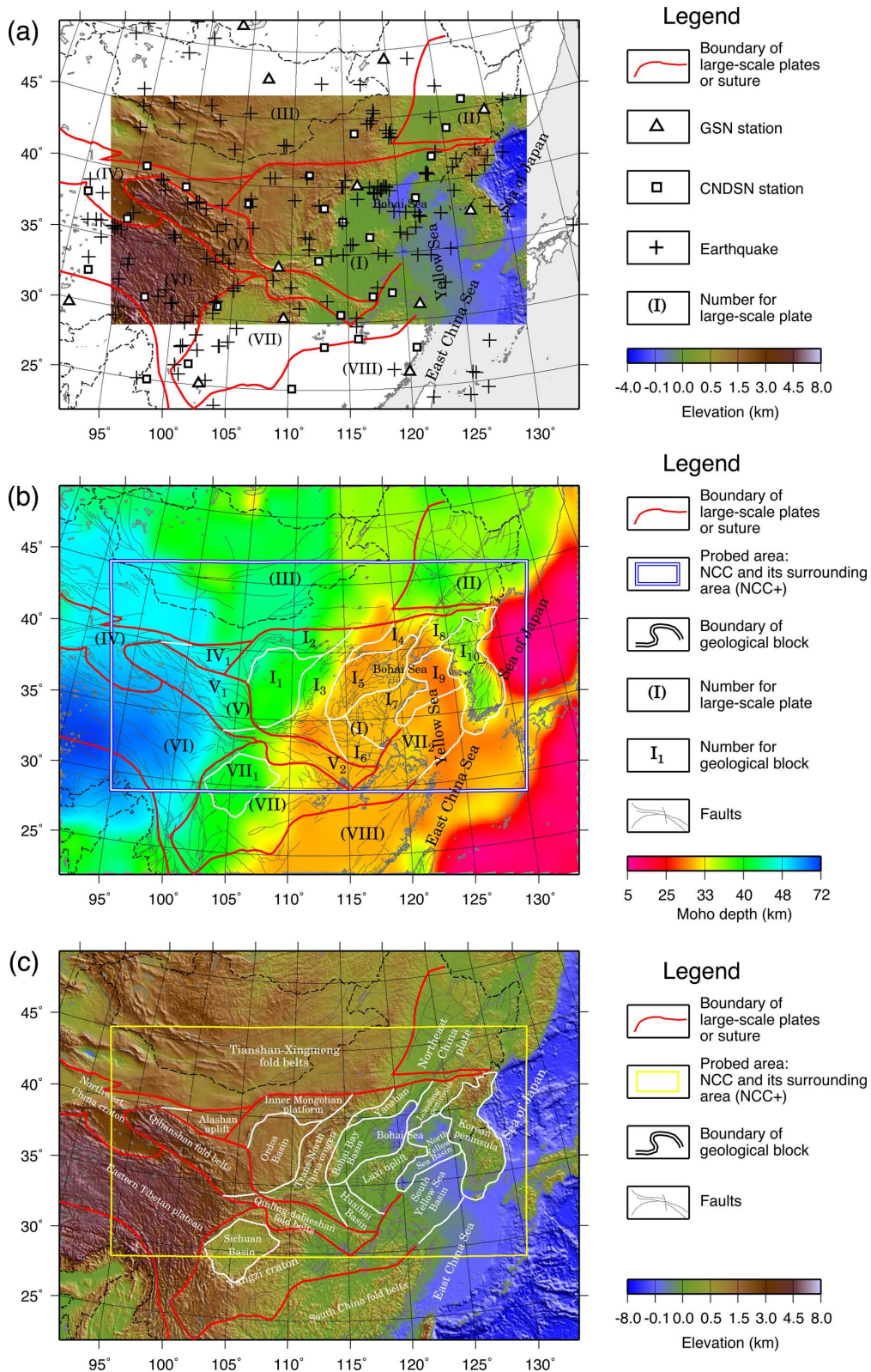
Figure 1. (a) An extended map showing locations of the CNDSN (solid squares) and GSN (triangles) stations, and the epicentres of selected earthquakes (crosses) used in this study, (b) the depth of the Moho discontinuity and (c) tomography. The coloured topography in (a), the white square in (b) and yellow square in (c) mark the region for *Lg* attenuation imaging. Also shown in (b) and (c) are main fault systems, and geotectonics in North China Craton and its surrounding regions (revised from Ma *et al.* 1989; Jun *et al.* 1996; Zhao *et al.* 2001; Huang *et al.* 2003; Hao *et al.* 2004). Note that both the number and name of these geological blocks are labelled in (b) and (c), respectively, and is also listed in Table 1.

velocity, attenuation, anisotropy and thermal structures in the crust and upper mantle can benefit our further understanding of the lithospheric evolution in the NCC.

The *Lg* wave is typically the most prominent seismic phase in high-frequency seismograms observed over continental paths at regional to teleseismic distances. It is usually understood as the sum of super critically reflected *S* waves trapped in the crust waveguide (Herrin & Richmond 1960; Bouchon 1982; Xie & Lay 1994) or as the surface wave overtones travelling in the continental crust (Knopoff *et al.* 1973; Mitchell 1995). An *Lg* wave can be blocked or strongly weakened when it propagates across oceanic crust or very thin continental crust, where the waveguide thickness changes rapidly. Weakened *Lg* waves can be observed in tectonically active regions where partial melting exists in the crust (e.g. Kennett 1986; Campillo 1987; Campillo *et al.* 1993; Xie & Lay 1994; Zhang & Lay 1995; Shapiro *et al.* 1996; Fan & Lay 2002, 2003a,b; Xie *et al.* 2004; Phillips *et al.* 2005; Pei *et al.* 2006; Zor *et al.* 2007; Ford *et al.* 2008; Mitchell *et al.* 2008; Pasyanos *et al.* 2009; Hong 2010; Zhao *et al.* 2010). *Lg* attenuation is closely related to the type of material, the degree of heterogeneity and the thermal status of the crustal waveguide. It can be quantified by a frequency dependent quality factor *Q*, one of the basic parameters that characterize the Earth's crust. Generally, high Q_{Lg} represents weak *Lg* attenuation and correlates well with a stable Archaean terrain, while low Q_{Lg} indicates strong *Lg* attenuation and corresponds to terrains with later geologic time or areas beneath which there are deep active faults (e.g. Fan & Lay 2002, 2003a,b; Xie *et al.* 2004, 2006; Zhao *et al.* 2010).

Early work addressing *Lg* attenuation in NCC was conducted by Jin & Aki (1988), who obtained a 1 Hz coda *Q* map (or described as *Lg* coda Q_0 map) for China. Using analogue seismic records, Ge *et al.* (1989) obtained the average regional *Q* values around 1.5 Hz of about 590 and 100 in the western and eastern NCC, respectively. Mitchell *et al.* (1997) investigated *Lg* coda *Q* across Eurasia and obtained a Q_0 image with a resolution lower than 10°. In their results, Q_0 was about 380 within the NCC. Both Cong *et al.* (2002) and Su *et al.* (2006) used *Lg* coda to calculate Q_0 in mainland China and adjacent regions. Their results revealed a relatively high Q_0 of 500 in the western NCC and a lower Q_0 of 200 in the eastern NCC, with a resolution lower than 10°. Phillips *et al.* (2005) used an amplitude ratio technique to investigate *Lg* attenuation in central and eastern Asia. For NCC, their regional Q_0 was about 400. On average, their result resolved *Lg* attenuation to 2.5°, with a peak resolution of 1.5°. Xie *et al.* (2006) measured *Lg* attenuation in eastern Eurasia and derived a laterally varying Q_0 model with resolutions between 4° and 10°. Their *Lg* attenuation model revealed the relation between the attenuation and geological activities in this region. In their model, a low-Q_{Lg} belt can be clearly seen starting from the Bohai Bay basin, crossing the Taihangshan range, stretching to the southern margin of Ordos basin, and finally entering into the Tibetan plateau. Mitchell *et al.* (2008) used more data to image *Lg* coda *Q* in Eurasia with their main result being similar to that of Xie *et al.* (2006). Both Pei *et al.* (2006) and Hearn *et al.* (2008) used amplitude data reported by the bulletin to image crustal attenuation up to a resolution of 1.5°. The resulting Q_0 distribution has similar patterns compared to those of Xie *et al.* (2006) but with systematically higher values. For example, in the Bohai Bay basin, their Q_0 is approximately 100 higher than those from Xie *et al.* (2006).

To the west and southwest of the NCC, there is the Northwest China Craton (refer to IV in Fig. 1), the Qinling–Qilianshan fold belts (V), the eastern Tibetan plateau (VI) and the Yangzi Craton (VII). In the Tibetan plateau, Xie *et al.* (2006) and Mitchell *et al.*

(2008) found the Q_0 values to be much lower than those in the NCC and Yangzi Craton. Fan & Lay (2002, 2003a,b) found the average Q_0 to be approximately 110 in eastern Tibet and 79–94 in northern Tibet, which is the most volcanically active area in Tibetan plateau (e.g. Turner *et al.* 1996). Owens & Zandt (1997) found that this region has inefficient *Sn* propagation, low *Pn* velocity and high Poisson's ratios of 0.34–0.35 in the top 30 km of the lithosphere. Those results suggested that partial melting existed in the crust, and was responsible for the observed strong *Lg* attenuation (Nelson *et al.* 1996; Rodgers & Schwartz 1998; Fan & Lay 2003a).

In this study, we use a large regional seismic dataset to develop a high-resolution broad-band *Lg*-wave attenuation model for the NCC and surrounding regions. It is expected that the model can benefit our understanding of the origin and evolution of the NCC. We also extend our investigation to a number of surrounding regions including part of the Northwest China Craton, the Qinling–Qilianshan fold belts, the eastern Tibetan plateau and the Yangzi Craton. We, therefore, will compare the crustal Q_{Lg} structures between the NCC and its surrounding regions.

2 DATA ANALYSIS

We collect 3517 broad-band vertical-component digital seismograms recorded at 39 stations from 176 regional events during 1999 December to 2010 May. The station and event parameters used in this study are listed in Tables S1 and S2 in the supplementary document, where the CNDSN station parameters are from Shen *et al.* (2008). The GSN and CNDSN stations are both equipped with broad-band instruments with nearly flat velocity responses between 0.03 and 8.0 Hz, and a sampling rate of 20, 40 or 50 per second. Fig. 1(a) shows the stations (triangles for GSN stations and squares for CNDSN stations) and events (crosses) used in this study. The probed region is highlighted by the coloured topography. Fig. 1(b) shows the Moho depth variation extracted from the $2° \times 2°$ global crustal model CRUST 2.0 (Bassin *et al.* 2000), while Fig. 1(c) gives an extend topography overlapped with names of major geological blocks. We require that the focal depth be shallower than the Moho discontinuity in order to select for crustal events only. Events with magnitudes between m_b 3.5 and 6.0 are selected to avoid complex rupture effects from large earthquakes. A minimum epicentral distance of 201 km is used to guarantee the development of a regional *Lg* wave. We visually check all traces to remove low quality data that was saturated, noisy, or had incorrect timing, which usually resulted from off scale records, low magnitudes, or the superposition of multiple events. Even though the selection process severely reduces the available data, a reasonable data set is obtained. Of all recordings, 83 per cent are between epicentral distances 200 and 2000 km. The maximum distance used is 2997 km.

As an example, Fig. 2 shows the observed seismograms from an earthquake that occurred on 2005 April 9. The waveforms are normalized vertical ground velocities, with their maximum amplitudes listed in micrometres per second ($\mu m\ s^{-1}$) on the left. Marked on these traces are apparent velocities in kilometres per second ($km\ s^{-1}$). Note that *Lg* waves arrive with an apparent velocity of 3.5 km s^{-1}. High frequency *Lg* waves are emphasized more at shorter epicentral distances and tend to be depleted at longer ranges. This indicates that measurements from short-distance stations are vital for obtaining high-quality high-frequency signals. The inset map shows great circle paths related to this data set with trace numbers labelled on individual paths. By visually inspecting the entire data set, we set the *Lg* group-velocity window to be 3.6–3.0 km s^{-1}. The noise series is picked before the first-arriving *P* wave (e.g. Zhao
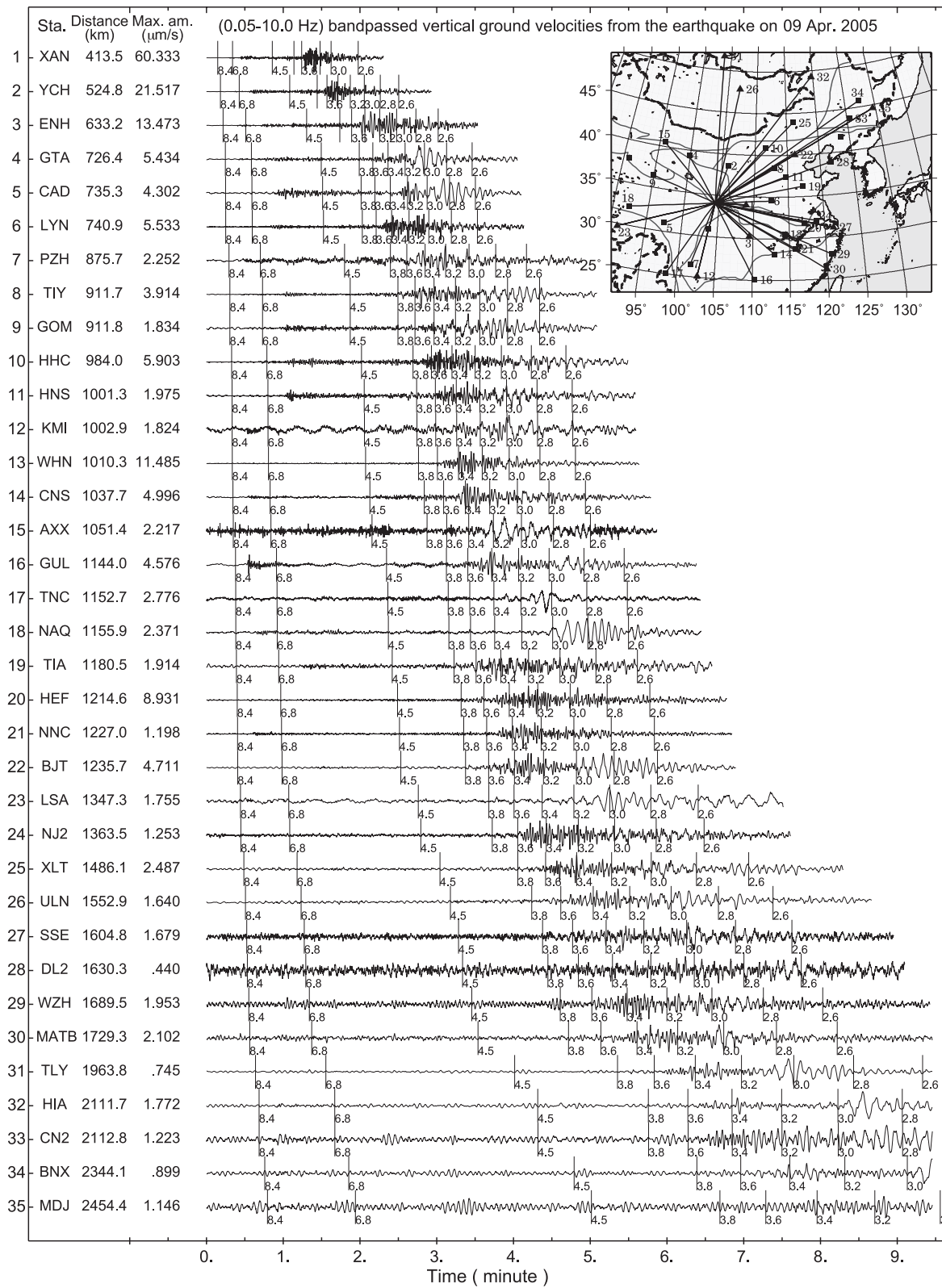
Figure 2. Sample records from an earthquake on April 9, 2005. Shown here are normalized vertical ground velocities (bandpass filtered between 0.05 and 10.0 Hz and ordered according to their epicentral distances). Station names and maximum amplitudes in micrometers per second are labelled on the left. Numbers on the waveforms indicate apparent group velocities. Note that the seismic *Lg* waves have an apparent group velocity of 3.5 km s^{-1}. The indexed map shows great circle paths from the epicentre to stations.
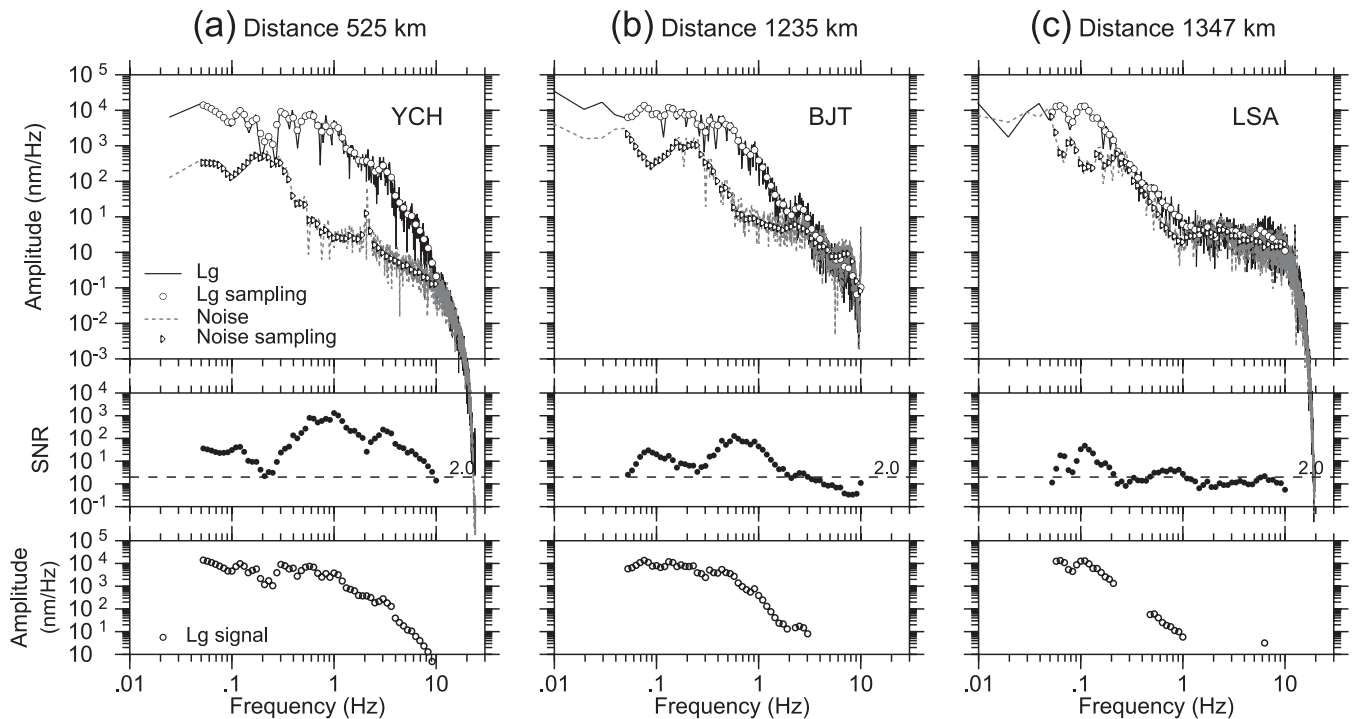
Figure 3. The *Lg*-wave spectra for stations (a) YCH, (b) BJT and (c) LSA. The raw *Lg*-wave spectra (circles) and noise spectra (triangles) are shown in the top row. The signal-to-noise ratios are shown in the middle row, while the noise-corrected *Lg*-wave spectra are illustrated in the bottom row. A threshold (dashed line) is used to eliminate the data with signal-to-noise ratio below 2.0.

et al. 2008). To obtain the *Lg*-wave spectra, we calculate Fourier spectra for both windowed *Lg* and the noise; sample their spectral amplitudes; and correct the *Lg* spectral amplitude by the noise spectrum (for details see Zhao *et al.* 2010).

We choose three stations from the data set shown in Fig. 2 and investigate their *Lg*-wave spectra. The epicentral distances to these stations are 524.8 km for YCH, 1235.7 km for BJT and 1347.3 km for LSA. The *Lg*-wave spectra from these stations are illustrated in the three columns in Fig. 3. Shown in the top row are original *Lg*-wave spectra (circles) and noise spectra (triangles) calculated at 58 frequencies distributed log evenly between 0.05 and 10.0 Hz. From these spectral amplitudes, we calculate signal-to-noise ratios, which are shown in the second row. We choose a threshold of 2.0 for the signal-to-noise ratio, which is marked in the second row using dashed lines. Illustrated in the bottom row are noise-corrected *Lg*-wave spectra where data points below the threshold have been dropped.

The data generally have good SNRs at low frequencies but as epicentral distance increases, their high-frequency content attenuates quickly. For example, at station YCH with a distance of 524.8 km, the corrected *Lg*-wave spectrum has high SNRs for the entire frequency band. At station BJT with a distance of 1235.7 km, the *Lg* signal above 2 Hz is more depleted than at YCH, resulting in poor SNRs at high frequencies. The epicentre distance for LSA is 1347.3 km, only slightly larger than for BJT. However, due to the very low Q_{Lg} values in the Tibetan plateau, the *Lg*-wave signal at LSA is severely weakened, leaving no available information above 1 Hz. This can also be seen by comparing waveforms from the two stations. As shown in Fig. 2, the record at BJT (trace 22) has stronger *Lg* wave relative to Rayleigh wave, while the *Lg* energy at LSA (trace 23) is nearly invisible. The above observations indicate that the high-frequency *Lg*-wave decays rapidly with the increase of distance, particularly in low-Q_{Lg} regions such as the

Tibetan plateau. The weak signals tend to be affected by noise. Beyond a certain distance, there will be no available high-frequency information above the noise level. Thus it is crucial to have high quality data from short-distance stations when we want to push *Lg* attenuation measurement to higher frequencies.

3 METHODOLOGY

Both a dual station method (Chun *et al.* 1987; Fan & Lay 2002, 2003a,b; Xie 2002; Xie *et al.* 2004, 2006; Zor *et al.* 2007; Bao *et al.* 2011) and a single station method (Xie 1993; Phillips *et al.* 2005; Pei *et al.* 2006; Ford *et al.* 2008; Mitchell *et al.* 2008; Pasyanos *et al.* 2009; Zhao *et al.* 2010) have been used in *Lg*-wave *Q* tomography. The single station method obtains the Q_{Lg} model by jointly inverting the attenuation and source terms. This method usually results in better data coverage particularly at higher frequencies but may introduce trade-offs due to the limited resolution between the attenuation and source terms. On the other hand, using the dual station method, the source terms are eliminated from the data before the inversion, thus reducing the trade-offs between the attenuation and source terms. However, the dual station method requires that the epicentre and two stations are roughly aligned. This severely limits the available data and reduces the spatial resolution of the Q_{Lg} inversion. In addition, the dual station data are usually collected from stations with much longer epicentre distances. As mentioned above, high-frequency signals are highly depleted at these distances, making the inversion of high-frequency attenuation extremely difficult. To reduce the trade-offs between the attenuation and source terms, while still resolving high frequency behaviour, the following strategy is used. We first apply the dual station method to obtain a low-resolution Q_{Lg} model. Next, using the low-resolution model as the initial model, we combine the dual- and single-station data together to invert the high-resolution broad-band Q_{Lg} model.

3.1 The initial model from the dual-station method

Following Xie *et al.* (2004), we extract the dual-station data for individual frequencies from the source-station data. At a given frequency f, the observed Lg-wave spectral amplitude A recorded at station i for event k can be expressed as

$$A_{ki} = S_k G_{ki} \Gamma_{ki} P_i R_{ki}, \tag{1}$$

where S_k is the source term, $G_{ki} = (\Delta_0 \Delta_{ki})^{-1\,2}$ is the geometrical spreading factor, which is from Street *et al.* (1975), and is adopted by previous investigators (e.g. Xie 1993; Benz *et al.* 1997; Pasyanos *et al.* 2009; Zhao *et al.* 2010), Δ_{ki} is the epicentral distance from event k to station i, and Δ_0 is a reference distance fixed at 100 km. The attenuation term can be expressed as

$$\Gamma_{ki}(f) = \exp\left[-\frac{\pi f}{V} \cdot \int_k^i \frac{ds}{Q(x,y,f)}\right], \tag{2}$$

where V is the Lg-wave group velocity, $\int_k^i ds$ is the integral along the great circle path from the event k to station i and $Q(x,y,f)$ is the Lg-wave quality factor, which is a function of the frequency f and the surface location (x,y). P_i is the site response, a factor related to local structures beneath stations. To well deal with the trade-offs between the attenuation and site amplification, we assume $\sum_{i=1}^N \log(P_i) = 0$, or neglect the site responses by letting $P_i = 1$, thus pushing the relative site term into the computed error term R_{ki}, which may be from any random effects in the Lg-wave propagation between earthquake k and station i (e.g. Xie 1993; Zhao *et al.* 2010), and calculate an apparent attenuation factor Q. In an ideal situation where two recording stations i and j are aligned with the source (Fig. 4a), the interstation amplitude A_{ij} can be obtained by calculating a scaled spectral ratio

$$A_{ij} = \frac{A_{kj}}{A_{ki}} = \left(\frac{\Delta_{kj}}{\Delta_{ki}}\right)^{-1/2} \exp\left[-\frac{\pi f}{V} \cdot \left(\int_k^j \frac{ds}{Q(x,y,f)}\right.\right.$$
$$\left.\left. -\int_k^i \frac{ds}{Q(x,y,f)}\right)\right]. \tag{3}$$

In an actual situation, the two stations may not be aligned perfectly (Fig. 4b) and certain tolerance is required. For example, Xie *et al.* (2004) used the azimuth difference of two stations, that is, the angle
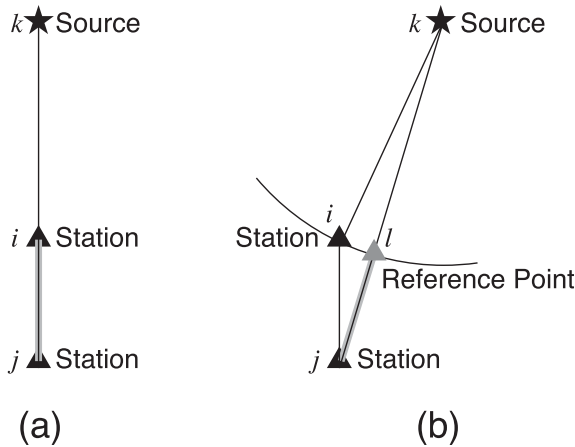
Figure 4. Schematics showing (a) an ideal geometry for dual-station method where the stations and the source are perfectly aligned, and (b) a more practical geometry where the source and stations are roughly aligned. To make the approximation valid, we require the distance between locations i and l smaller than half of an inversion grid.

ikj in Fig. 5(b), as the judgment and set a maximum tolerance of $15°$. Here we use a slightly different criterion. We set a reference point l on the ray path kj, with its distance kl equals to the distance ki (see Fig. 5b). Then, we set a tolerance by requiring the distance between points i and l to be within a half-grid space. For stations, which met this criterion, their interstation amplitude is approximated as

$$A_{ij} = \frac{A_{kj}}{A_{ki}} \approx \left(\frac{\Delta_{kj}}{\Delta_{ki}}\right)^{-1/2} \cdot \exp\left[-\frac{\pi f}{V} \cdot \int_l^j \frac{ds}{Q(x,y,f)}\right]. \tag{4}$$

At each frequency, we use (eq. 4) to calculate an average regional Q_{Lg} model. Fig. 5 illustrates the dual station data at selected frequencies. The crosses in each panel denote the corrected interstation amplitudes $\ln[A_{ij}(\Delta_{kj}/\Delta_{ki})^{1/2}]$ versus distance Δ_{ij}. As mentioned above, Lg waves tend to be depleted at larger distances, particularly for high-frequency signals. Beyond certain epicentral distances, high-frequency Lg signals easily fall below the noise level. Following Zhao *et al.* (2010), we use a frequency dependent truncation distance to further quality control the Lg data. Under a given frequency the data obtained beyond the truncation distance are excluded (Zhao *et al.* 2010). After applied the truncation distance to control quality, we use dual-station date to statistically calculate the average Q_{Lg} as an initial model for our joint inversion. Fig. 5 illustrates the data at selected frequencies. For frequencies above 2 Hz, any certain data points, which are apparently contaminated by the noise have been eliminated based on truncation distance. Thus, the data quality is effectively improved.

3.2 The *Lg Q* tomography by jointly using both dual- and single-station data

In this section we introduce an Lg Q tomography by jointly using the dual- and source- station data. It is expected that this method can reduce the attenuation-source trade-offs to a certain extent within a given seismic network, and improve the resolution at high frequencies.

Zhao *et al.* (2010) proposed a single-station scheme for simultaneously inverting the Q_{Lg} and the source function. Perturbation theory is used to linearize the relationship among the Q_{Lg} model, the source function, and the observed Lg-wave spectrum

$$\mathbf{H} = \mathbf{A} \cdot \delta\mathbf{Q} + \mathbf{E} \cdot \delta\mathbf{U}, \tag{5}$$

where $\mathbf{H}$ is a vector composed of residuals between the observed and the synthesized Lg spectra, $\delta\mathbf{Q}$ is a vector composed of the perturbations of the Q model, matrix $\mathbf{A}$ sets up the relationship between Q perturbations and the observed Lg-wave spectra, $\delta\mathbf{U}$ is a vector composed of the perturbations of the source term, and matrix $\mathbf{E}$ sets up the relationship between the source perturbations and the observed Lg-wave spectra. Similarly, from (eq. 4), we can create a linear system

$$\mathbf{H_d} = \mathbf{A_d} \cdot \delta\mathbf{Q} \tag{6}$$

to relate the Q model to the dual-station data, where $\mathbf{H_d}$ is a vector composed of residuals between observed and synthetic spectral ratios, and the matrix $\mathbf{A_d}$ can be obtained by descretizing (eq. 4). Combining (eq. 5) and (eq. 6), we obtain a hybrid tomography equation

$$\begin{bmatrix} \mathbf{H} \\ \mathbf{H_d} \end{bmatrix} = \begin{bmatrix} \mathbf{A} \\ \mathbf{A_d} \end{bmatrix} \cdot \delta\mathbf{Q} + \begin{bmatrix} \mathbf{E} \\ 0 \end{bmatrix} \cdot \delta\mathbf{U}. \tag{7}$$

To solve the inverse problem, we start from a unit source function and a constant initial Q_{Lg} obtained by linear regression of
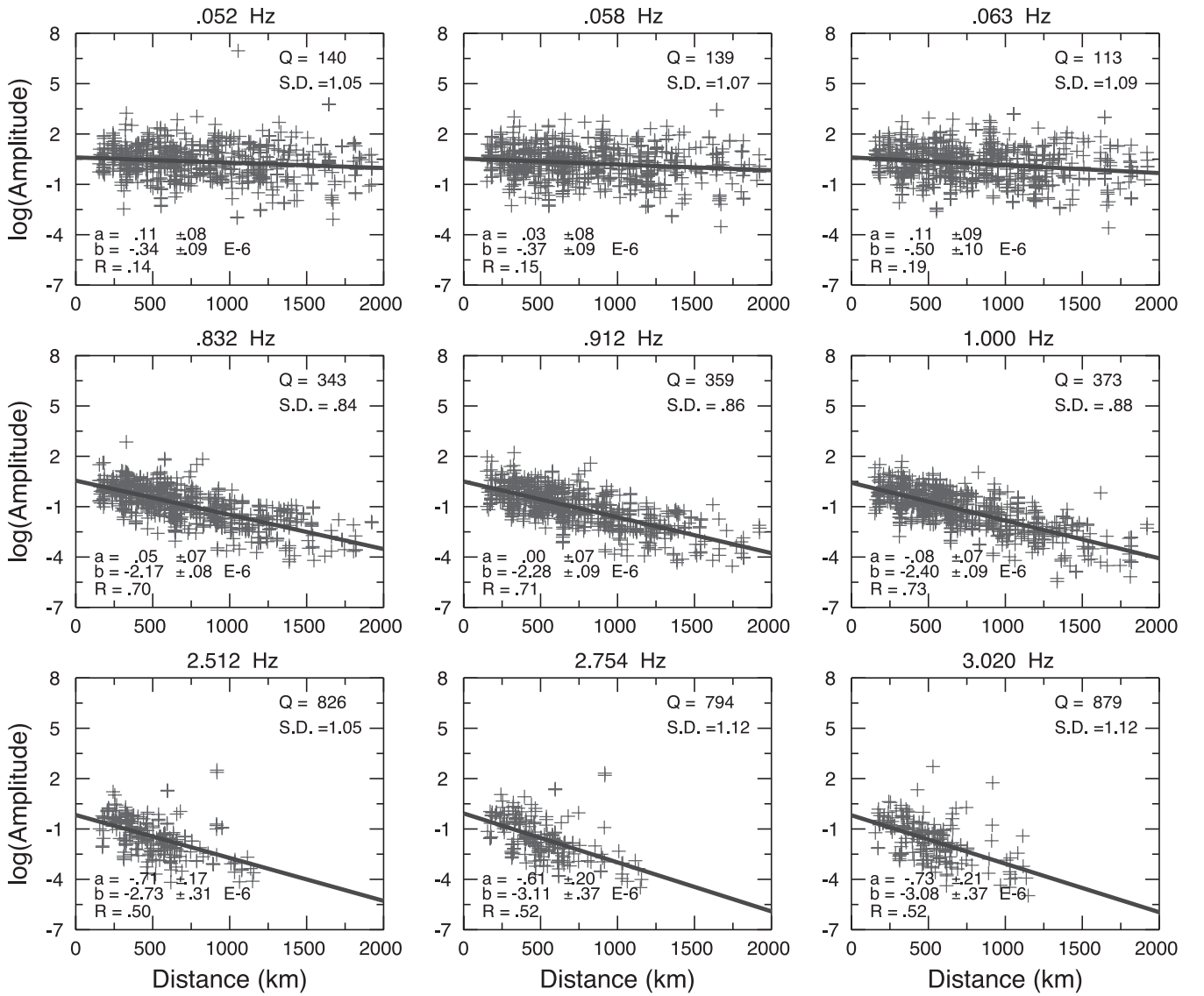
Figure 5. Corrected dual-station spectral ratios versus the interstation distance at selected frequencies. Crosses are data after corrected by the geometrical spreading, and solid lines are their linear regressions. Regional average Q_{Lg} values are calculated from the slopes of these lines and labelled in each panel.

dual-station data (i.e. the regression lines in Fig. 5). The LSQR algorithm with regularization, damping, and smoothing is employed to solve the linear system (eq. 7; Paige & Saunders 1982; Phillips *et al.* 2000). At each step, we solve for perturbations $\delta\mathbf{Q}$ and $\delta\mathbf{U}$ by minimizing $[\mathbf{H}\ \mathbf{H}_d]^T$. These perturbations are used to update the attenuation model and source terms. Due to the nonlinear property of the problem, iterations are required. By inverting independently for individual frequencies we obtain a high-resolution and broad frequency band *Lg* attenuation model and the *Lg* source functions. In addition, an alternative parameterization can be used based on Q^{-1} and source term. Thus, it is easy to build a linear equation for solving Q^{-1} and source term simultaneously. Its resolving ability needs additional work to detect.

3.3 The resolution test

We use the checkerboard method for resolution analysis in our *Lg*-wave Q tomography (e.g. Zelt 1998; Morgan *et al.* 2002; Al-Damegh *et al.* 2004; Zhao *et al.* 2010). Because the signal-to-noise

ratios and the truncation distances are all dependent on frequencies, the available data points are different, resulting in different resolution at different frequencies. Thus, we conducted resolution analyses independently at individual frequencies. We first create a trial *Lg* attenuation model by superimposing checkerboard-shaped positive and negative perturbations on a constant background Q_{Lg}. The Q_{Lg} perturbation is 7 per cent relative to the background Q_{Lg}. Then, we use (eq. 1) to generate a synthetic source-station *Lg* spectral data set, where epicentres and station locations are from the actual observation geometry, and the source terms are calculated using the seismic moment M_0 and the corner frequency f_c estimated from the observed magnitude using empirical relations (Zhao *et al.* 2010). At each frequency, only events and stations that actually provide data above the signal-to-noise ratio threshold are used to generate test data. To simulate the noise in real data, a 5 per cent root mean square fluctuation is added to the test data. Next, we extract the dual-station data from source-station data according to the half-grid-space criterion mentioned above. Linear regression is applied to dual-station data to obtain a regional
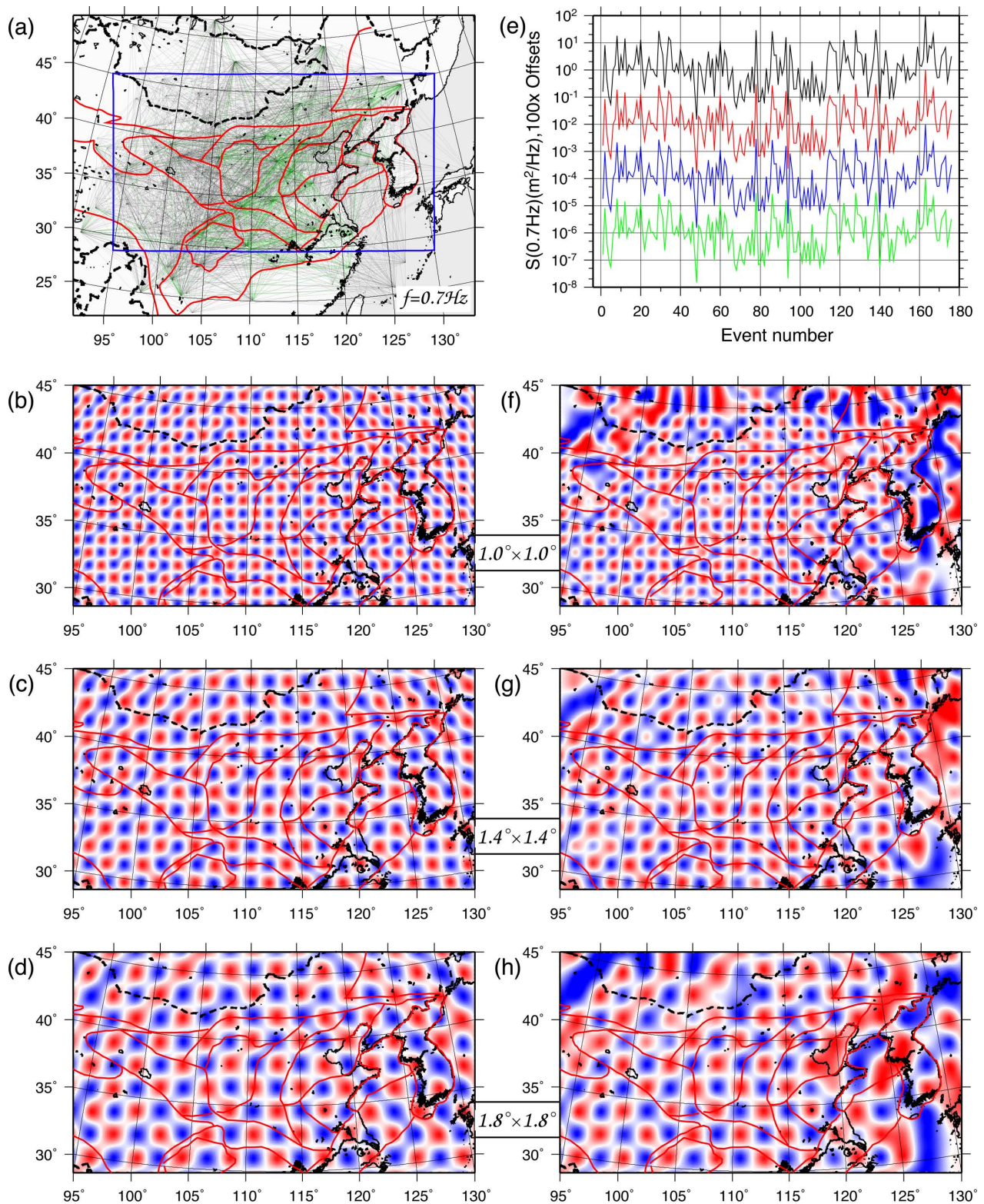
Figure 6. Resolution analysis at 0.7 Hz. (a) Ray path coverage, where black and green lines are for single- and dual-station data, respectively. (b)–(d) are initial checkerboard Q_{Lg} models with grid sizes $1° \times 1°$, $1.4° \times 1.4°$ and $1.8° \times 1.8°$. Shown in (e) are input (black) and retrieved Lg-wave excitation functions for $1° \times 1°$ (red), $1.4° \times 1.4°$ (blue) and $1.8° \times 1.8°$ (green) grids. (f)–(h) are retrieved checkerboard Q_{Lg} perturbations with different resolutions.

average Q_{Lg} model which is used as the initial model. Finally, we invert the dual- and single-station data simultaneously, and compare the results with the checkerboard Q_{Lg} model and the input source functions.

As an example, Fig. 6 demonstrates the resolution analysis at 0.7 Hz. Shown in Fig. 6(a) are both 3299 source-station ray paths (black lines) and 1044 interstation ray paths (green lines). Apparently, there is denser ray coverage in the NCC than in the surrounding
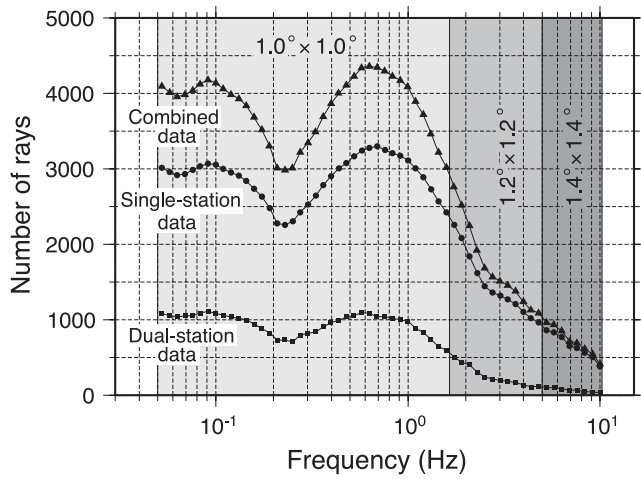
Figure 7. Number of rays for frequencies 0.05–10.0 Hz, along with resolutions from checkerboard analyses.

regions and the single-station data have a much better coverage than the dual-station data. Figs 6(b)–(d) illustrate the $1° × 1°$, $1.4° × 1.4°$ and $1.8° × 1.8°$ checkerboard test models, which are formed by superimposing ±7 per cent Q perturbations on a constant background model of Q (0.7 Hz) = 362. Fig. 6(e) illustrates the 176 source functions at 0.7 Hz, where the black line at the top is the pre-assigned source functions calculated from empirical moment-magnitude relations, and the red, blue and yellow lines show the retrieved source functions corresponding to the three checkerboard test models, respectively. The consistency between the four groups of numbers indicates the source functions are properly retrieved. Figs 6(f)–(h) illustrate the reconstructed Q_{Lg} models with different spatial grids. Comparing the original checkerboard patterns (Figs 6b–d) with the retrieved results, we see that the perturbation patterns are better resolved in NCC compared to surrounding areas and are consistent with the ray coverage. From the result, the perturbation patterns appear to be better reconstructed in a coarser grid, while a finer grid provides higher resolution. The $1.4° × 1.4°$ and $1.8° × 1.8°$ grids reproduce the checkerboard patterns for the entire region except for some border areas; however, they do not provide enough resolution to reveal the relationship between the attenuation and regional tectonics. The $1° × 1°$ grid appears to have the optimal trade-off between the resolution and the reliability for 0.7 Hz data. Limited by the available data, a trade-off should be made to balance the inversion resolution and reliability. We conduct resolution

tests for all 58 individual frequencies by using a series of checkerboard models with grid sizes varying from $0.6° × 0.6°$ to $2° × 2°$ at an increment of $0.2°$. By using visual inspection, we obtain the resolution estimations at individual frequencies. Fig. 7 summarizes the numbers of available rays (for single-station, dual-station and combined data sets) versus frequency, with the shading illustrating the estimated resolutions for particular frequencies obtained by resolution analyses.

4 TOMOGRAPHIC RESULTS

Based on our data and inversion methods discussed above, we obtain a broad-band *Lg* attenuation model in and around the NCC at 58 discrete frequencies between 0.05 and 10.0 Hz. Simultaneously, we obtain the source spectra for 176 selected events. At each frequency, we calculate a total of 150 iterations, and the result is chosen from the iteration, which has the smallest residual error. As an example, Fig. 8(a) shows the convergence curve for 0.7 Hz. The smallest residual of 0.515 appeared at the 98th iteration. Compared to the starting residual of 1.433, the rms error is reduced by about 64 per cent. Fig. 8(b) summarizes all rms residuals at 58 frequencies. The remaining error may result from source complications, site responses, and other random effects, which are neglected in our joint inversion.

4.1 Q_{Lg} distributions

Illustrated in Fig. 9 are Q_{Lg} distributions, ray path coverage, and resolution analysis at 0.5 and 1.0 Hz, respectively. Also shown in Figs 9(a) and (d) are the major geological sutures (white lines), active fault systems (thin black lines), and locations of $m_b > 6.0$ earthquakes from the USGS catalogue (red circles). Note that different colour scales are used for two frequencies. The most prominent feature in these resulting Q_{Lg} maps is that high-frequency Q_{Lg} is generally higher than the lower frequency values. The lateral Q variations are consistent with the tectonic structures in and around the NCC (referred as NCC+ in Fig. 1). The boundary of the NCC [referred as (I) in Fig. 1] is mostly defined by strong Q_{Lg} gradients, especially for the western, southern, and eastern boundaries at 0.1–1.0 Hz. The Sichuan basin (VII_1) belongs to the Yangzi Craton (VII), but had similar Q_{Lg} with the Ordos basin. The Trans-North China orogen (Central NCC, I_3), which consists of the Taihangshan range, had relatively low Q_{Lg} values at 2.0 Hz. Some Q_{Lg} differences are also observed between eastern and western mountain
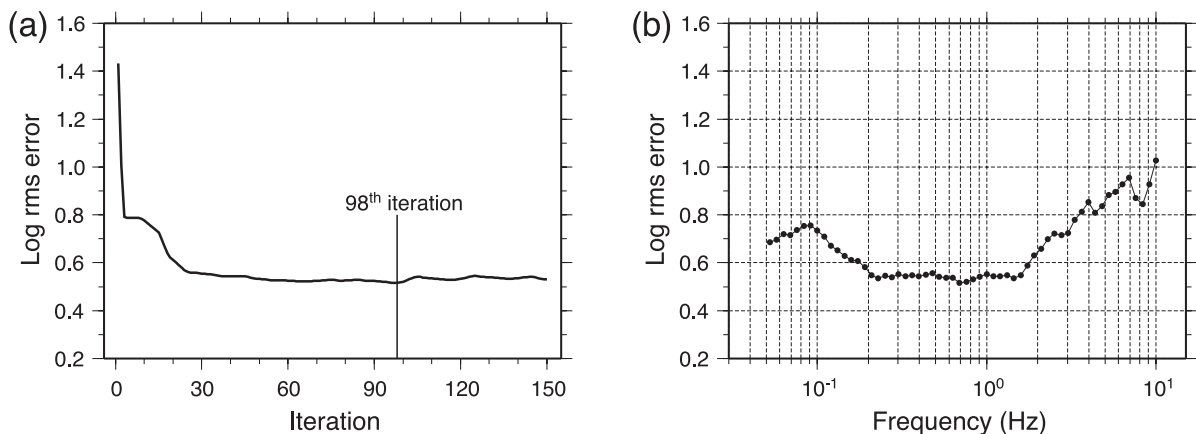
Figure 8. (a) An illustration showing the iteration procedure for 0.7 Hz Q_{Lg} inversion, and (b) all 58 rms residuals at individual frequencies.
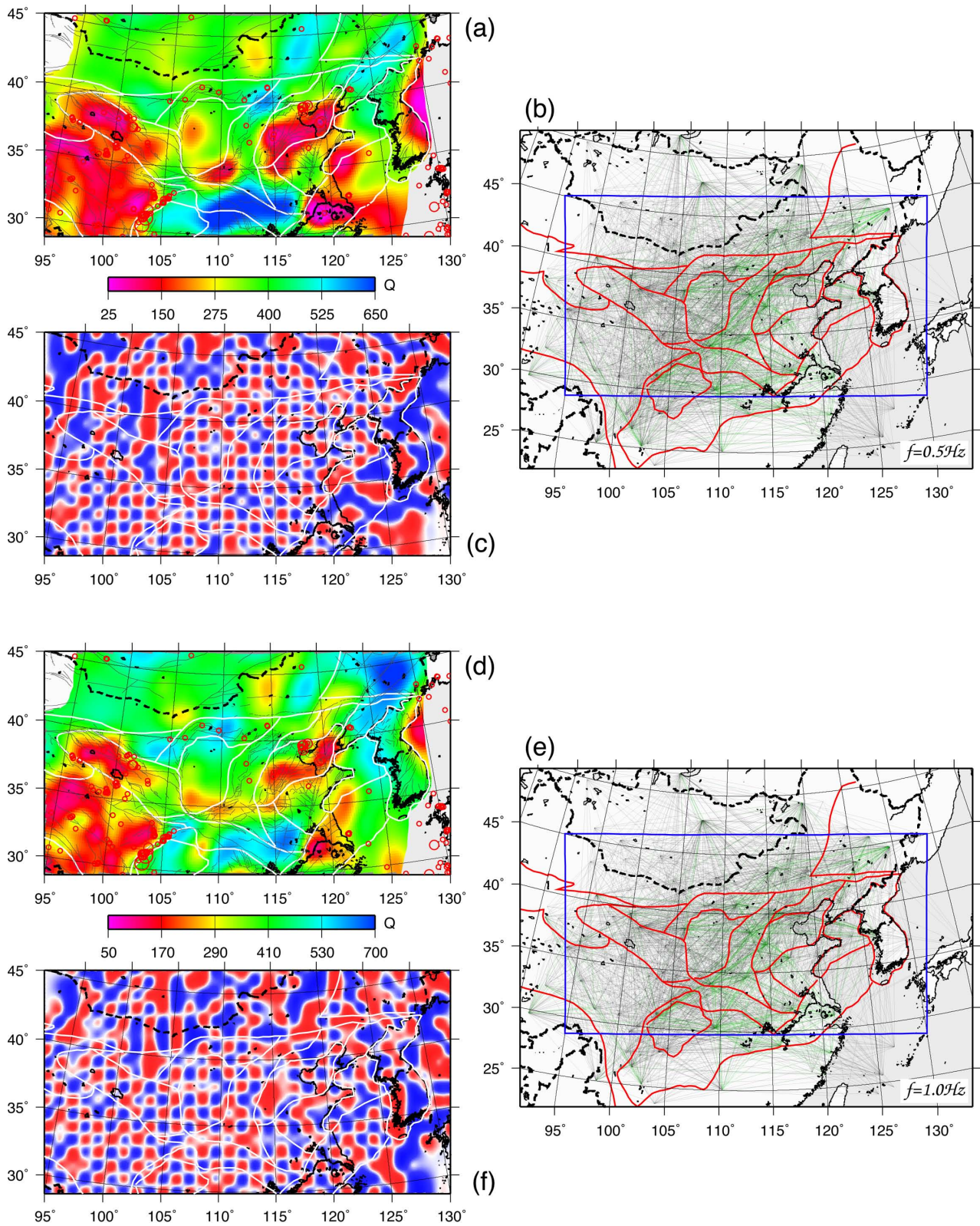
Figure 9. Q_{Lg} distributions, ray path coverage, and spatial resolutions at frequencies 0.5 (a)–(c) and 1.0 Hz (d)–(f), respectively. In Figs (a) and (d), the important geological boundaries, fault systems and earthquakes larger than m_b 6.0 are also labelled.

areas. In eastern uplifted regions, the Qinling-Dabieshan fold belts (V_2) has high Q_{Lg} values, while relatively low Q_{Lg} values occur in both the Eastern Tibetan plateau (VI) and Qilianshan fold belts (V_1). Many large earthquakes are located in regions where there

are low Q_{Lg} values or strong Q_{Lg} variations. For example, the 1976 Tangshan earthquake, the 2008 Wenchuan earthquake, and their aftershocks occurred in belts where Q_{Lg} between 0.1 and 5.0 Hz varies abruptly.
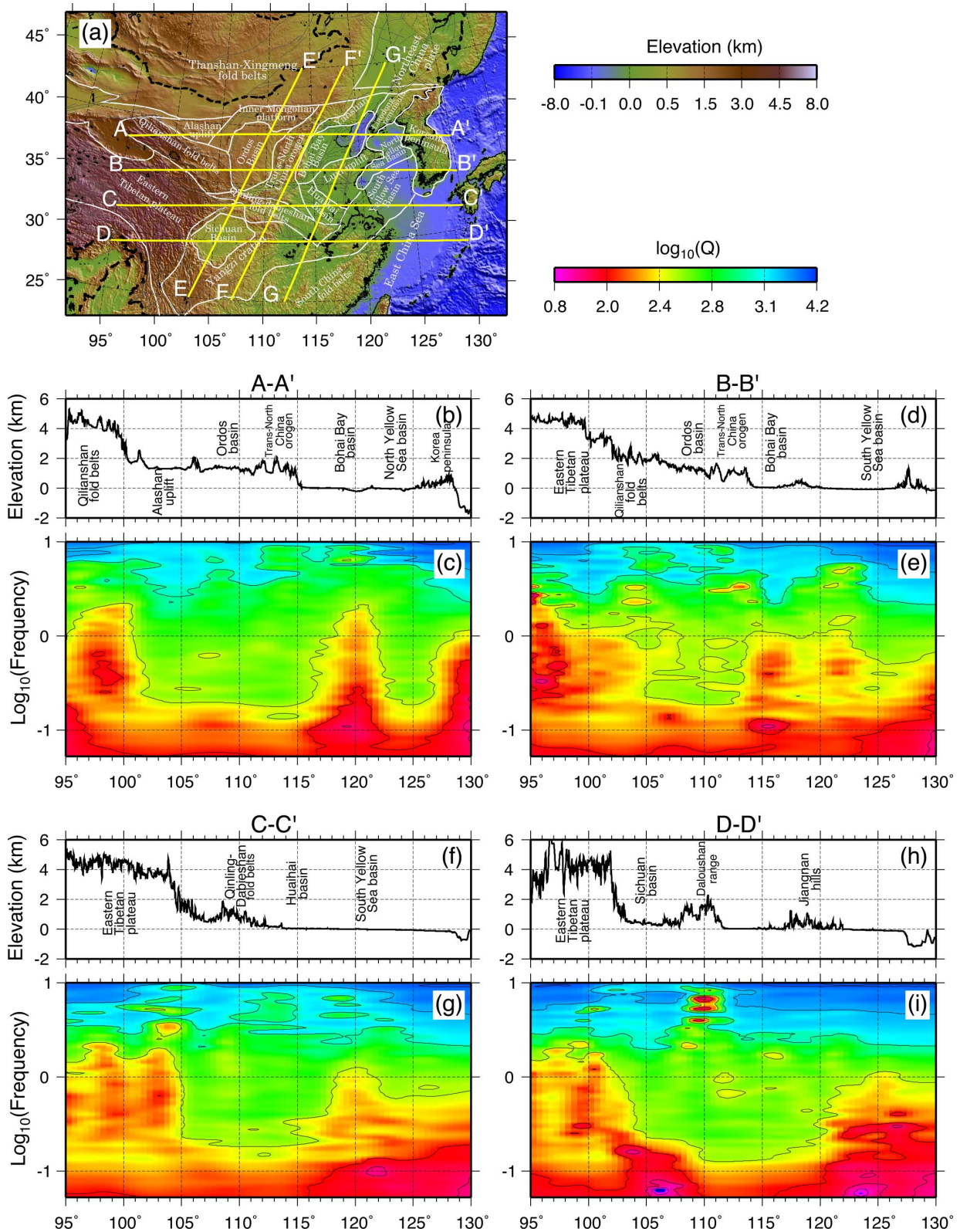
Figure 10. Corss-sections of topography and Q_{Lg} versus frequency. (a) Map showing locations of these cross-sections. (b)–(i) Latitudinal sections, and (j)–(p) Longitudinal sections.

To illustrate Q_{Lg} versus frequency, we calculate attenuation along selected cross-sections. Fig. 10(a) illustrates the locations of seven great circle segments, in which the four latitudinal sections are labelled by A–A′ to D–D′, and the three longitudinal sections are labelled by E–E′ to G–G′. Shown in Figs 10(b)–(p) are Q_{Lg} profiles versus frequency, along with the elevations for these sections. Cross-section A–A′ is located along the northern border of the NCC. From west to east, it successively crosses 7 geological blocks with
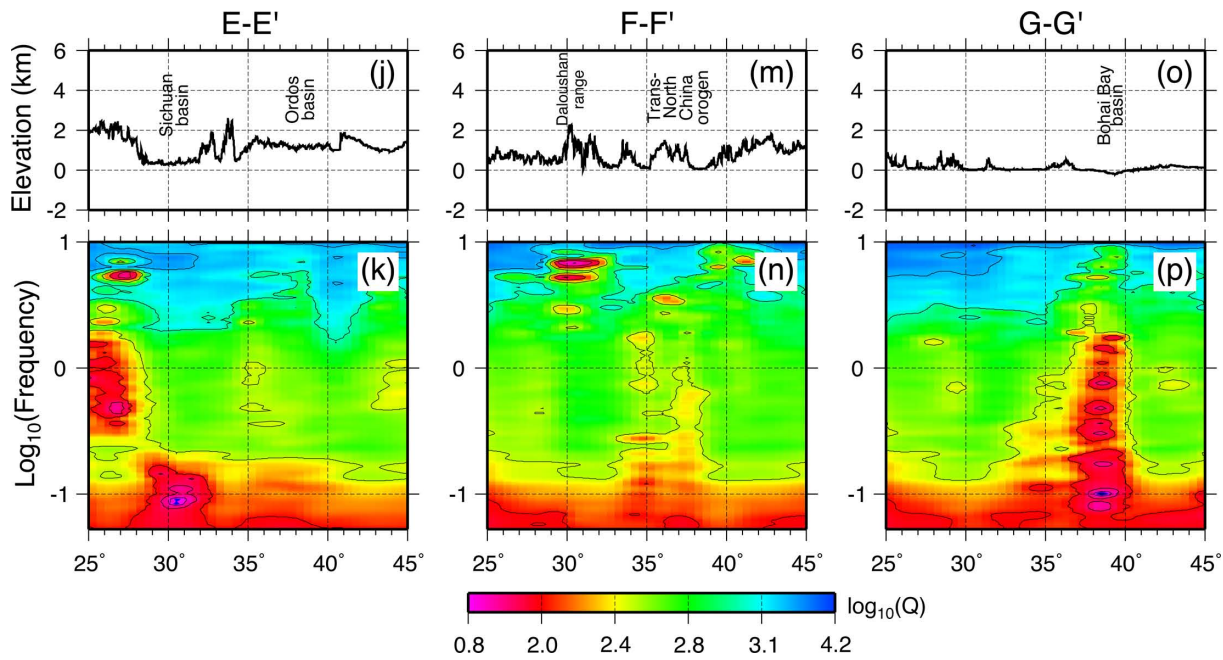
Figure 10. (*Continued.*)

the elevation decreasing (Fig. 10b). As shown in Fig. 10(c), three apparent low Q_{Lg} (0.2–2.0 Hz) regions correspond to the Qilianshan fold belts (V_1), the Bohai Bay basin (I_5), and the oceanic area to the east of the Korea peninsula. Next, the cross-section B–B′ crosses six geological blocks as shown in Fig. 10(d). The low Q_{Lg} (0.2–5.0 Hz) anomalies arise in west plateau areas for both the Eastern Tibetan plateau and the Qilianshan fold belts, in east basin regions for Bohai Bay basin (I_5), and South Yellow Sea basin (VII_2). On the section C–C′, relatively low Q_{Lg} (0.2–2.0 Hz) values are observed in the Eastern Tibetan plateau (VI) with high elevation and South Yellow Sea basin (VII_2) with low elevation, as shown in Figs 10(f) and (g). The section D–D′ is mainly located in the Eastern Tibetan plateau and the Yangzi Craton (VII). In Fig. 10(i), low Q_{Lg} (0.2–2.0 Hz) anomalies were seen in the Eastern Tibetan plateau and East Sea regions. The E–E′ section illustrates that the Yungui plateau has relatively low Q_{Lg} values (0.2–5.0 Hz), while stable Q_{Lg} (0.2–10.0 Hz) values arise in other regions including the Sichuan and Ordos basins (Fig. 10k). Section F–F′ is roughly overlapped with the north-south gravity lineament (Chen & Ai 2009). Fig. 10(n) shows a relatively uniform Q_{Lg} but it drops slightly near the Bohai Bay basin (I_5). Section G–G′ in Fig. 10(p) reveals strong attenuation in the Bohai Bay basin (I_5). These cross-sections show the lateral variations of the broad-band Q_{Lg}. The regional differences are mainly observed between 0.2 and 2.0 Hz. At frequencies lower than 0.2 Hz or higher than 5 Hz, regional differences become less pronounced. In Fig. 10, the Q_{Lg} increasing with frequency clearly shows that the geometric spreading is faster than the initial assumption (Street *et al.* 1975). *Lg* wave could be leaking into the mantle and scattered within the crust, so that the geometric spreading bias would lead to underestimate Q values (Benz *et al.* 1997). However, at frequencies around 1 Hz, our Q_{Lg} model agrees with previous narrow band results. Fan & Lay (2002, 2003a,b) found the average Q_0 for Eastern Tibet to be approximately 110. Xie *et al.* (2006) and Mitchell *et al.* (2008) obtained lower Q_0 values in Tibet than in the NCC and Yangzi Craton. Strong *Lg* attenuation in the Bohai Bay basin was observed by Phillips *et al.* (2000) and Pei *et al.* (2006).

In order to characterize the *Lg* attenuation for different geological formations, we use the statistical method to investigate variations of the frequency dependent Q_{Lg} in different geological units, including the large-scale terranes, basins, mountains and fold belts (Zhao *et al.* 2010). For each geological block, we calculate average Q_{Lg} at 58 individual frequencies. For the entire investigated region (NCC+), the average Q_0 is 349 with lower and upper standard deviations of 236 and 516. The average Q_0 values are 374 (273–512) for NCC and 188 (124–286) for Eastern Tibetan plateau (VI), much lower than the regional average. The Qinling-Qilianshan fold belts (V) is fully included in the probed region with an average Q_0 of 321 (280–497). The average Q_0 values are listed in Table 1 with standard deviations. The variations of average Q_0 values between these first-order geological units reveal significant differences in crustal attenuation, while relatively large standard deviations indicate strong internal variations.

As shown in Figs 1(b) and (c), the NCC can be briefly divided into ten geological blocks: the Ordos basin (I_1), the Inner Mongolian platform (I_2), the Trans-North China orogen (I_3), the Yanshan range (I_4), the Bohai Bay basin (I_5), the Huaihai basin (I_6), the Luxi uplft (I_7), the Liaodong peninsula (I_8), the North Yellow Sea basin (I_9) and the Korea peninsula (I_{10}). Both the Ordos basin (I_1) and Inner Mongolian platform (I_2) are affiliated with the west NCC (WNCC). Their average Q_0 values are 393 (309–500) and 461 (390–544), respectively. Zhao *et al.* (2010) reported that the average Q_0 values were 375 (224–627) for the Songliao basin, and 675 (559–814) and 630 (459–864) for the Daxinganling and Changbaishan ranges, respectively. From our result, the Q_0 difference between northeastern and western basins is small, while the Q_0 of the western mountains is apparently lower than that of northeastern mountains. The Trans-North China orogen (I_3) is located in the central NCC (CNCC) and overlaps a north–south gravity lineament. The CNCC block has a relatively low Q_0 of 361 (299–436) as compared to that of 421 (337–527) in WNCC. The rest of the geological blocks (I_4–I_{10}) belong to the east NCC (ENCC), where the lowest average Q_0 is 249 (173–359) located in the Bohai Bay basin (I_5). This

Table 1. *Lg Q* and heat flow models for individual geological blocks.

Geological block name	Geological block number	CRUST2.0 model Crust thickness (km)	Q_0 (1 Hz Q)	η (0.5–1.5 Hz)	Q (0.2–1.0 Hz)	Heat flow model[a] Heat flow (mW m^{-2})	Type of block	Symbol[b] in Figs 12 and 13
NCC and its surrounding area	NCC+	40.0 ± 11.8	349 (236–516)	0.49 ± 0.03	267 ± 30	61.03 ± 13.97	Integrated	○, □
NCC	I	34.7 ± 5.1	374 (273–512)	0.41 ± 0.03	298 ± 30	61.42 ± 13.33	Integrated	○
Northeast China Plate	II	36.9 ± 2.5	506 (406–632)	0.36 ± 0.03	376 ± 63	75.36 ± 16.43	Integrated	○
Tianshan–Xingmeng fold belts	III	44.1 ± 5.2	424 (364–496)	0.44 ± 0.04	348 ± 26	66.25 ± 9.75	Integrated	○
Northwest China craton	IV						Integrated	○
Qinling–Qilianshan fold belts	V	44.8 ± 10.1	321 (208–497)	0.32 ± 0.02	272 ± 17	62.92 ± 15.28	Integrated	○, □
Eastern Tibetan plateau	VI	60.2 ± 7.6	188 (124–286)	0.52 ± 0.02	148 ± 11		Mountains	△, □
Yangzi Craton	VII					62.09 ± 14.23	Integrated	○
South China fold belts	VIII						Integrated	○
Ordos basin	I$_1$	41.4 ± 1.4	393 (309–500)	0.39 ± 0.04	347 ± 13	61.75 ± 8.05	Basin	▽
Inner Mongolian platform	I$_2$	43.7 ± 3.1	461 (390–544)	0.40 ± 0.05	404 ± 18		Mountains	△
Trans-North China orogen	I$_3$	34.9 ± 4.7	356 (290–438)	0.16 ± 0.03	345 ± 13	58.68 ± 14.63	Mountains	△
Yanshan	I$_4$	31.9 ± 1.8	388 (318–474)	0.10 ± 0.06	396 ± 19	63.98 ± 13.13	Mountains	△
Bohai Bay basin	I$_5$	31.0 ± 1.0	249 (173–359)	0.49 ± 0.01	180 ± 31	62.23 ± 11.97	Basin	▽
Huaihai basin	I$_6$	31.0 ± 0.0	447 (308–649)	0.34 ± 0.06	354 ± 64	61.85 ± 16.29	Integrated	○
Luxi uplift	I$_7$	31.0 ± 0.0	321 (261–395)	0.63 ± 0.05	230 ± 31	71.80 ± 13.85	Integrated	○
Liaodong peninsula	I$_8$	34.1 ± 3.3	535 (450–637)	0.25 ± 0.03	415 ± 67	57.12 ± 14.68	Mountains	△
North Yellow Sea basin	I$_9$	30.1 ± 1.1	390 (299–508)	0.42 ± 0.01	307 ± 25		Basin	▽
Korea peninsula	I$_{10}$	34.1 ± 3.1	412 (328–519)	0.62 ± 0.02	275 ± 56		Integrated	○
West NCC	WNCC (I$_1$ and I$_2$)	42.3 ± 2.5	421 (337–527)	0.39 ± 0.04	372 ± 14	64.11 ± 6.39	Integrated	○
Central NCC	CNCC (I$_3$)	34.7 ± 4.7	361 (299–436)	0.17 ± 0.03	347 ± 15	59.98 ± 14.59	Mountains	△
East NCC	ENCC (I$_4$–I$_{10}$)	31.5 ± 1.9	337 (227–500)	0.41 ± 0.03	258 ± 38	62.28 ± 14.01	Integrated	○
Alashan uplift	IV$_1$	49.5 ± 1.3	396 (269–583)	0.27 ± 0.02	331 ± 32	50.83 ± 16.64	Mountains	△, □
Qilianshan fold belts	V$_1$	51.2 ± 6.0	253 (175–366)	0.51 ± 0.02	196 ± 15	72.18 ± 13.67	Mountains	△, □
Qinling–dabieshan fold belts	V$_2$	33.0 ± 2.4	454 (352–585)	0.01 ± 0.03	449 ± 36	54.58 ± 11.34	Mountains	△
Sichuan basin	VII$_1$	41.1 ± 1.9	416 (348–497)	0.17 ± 0.03	376 ± 42	57.16 ± 7.92	Basin	▽
South Yellow Sea basin	VII$_2$	30.5 ± 1.0	309 (218–436)	0.75 ± 0.01	217 ± 26	68.70 ± 9.45	Basin	▽

[a]From Wang & Huang (1990) and Hu *et al.* (2001).

[b]□, related to Tibetan plateau.

result is higher than the previous result by Zhao *et al.* (2010), where the Bohai Bay basin is only partially included. Thus, the current result should be more reliable. The highest average Q_0 of 535 (450–637) appears in mountainous Liaodong peninsula (I$_7$). The North Yellow Sea basin (I$_8$) has an average Q_0 of 390 (299–508). The Korea Peninsula (I$_9$) has a relatively high Q_0 of 412 (321–518). The average Q_0 values for the ENCC, CNCC, and WNCC are 337(227–500), 361(299–436) and 421(337–527) (Table 1), respectively. An apparent tendency of increasing Q_0 can be seen from east to west. For three basins, the Ordos basin, Sichuan basin, and Bohai Bay basin, the average Q_0 values are 393(309–500), 416(348–497) and 249(173–359), respectively. The similar Q_0 values in the Ordos and Sichuan basins may indicate that there are similar *Lg* attenuation mechanisms for these western basins. On the other hand, the big difference between the western and eastern basins may imply different underlying attenuation mechanisms. These features are also supported by previous investigators (Xie *et al.* 2006; Mitchell *et al.* 2008).

From the broad-band tomographic model for *Lg* attenuation in NCC, we found that not only Q_0, but also Q values between 0.2 and 1.0 Hz can well characterize the different geological blocks. Fig. 11 is a low-frequency band map showing mean Q distribution between 0.2 and 1.0 Hz. Compared to Q_0 distribution (Fig. 9d), similar features can be seen in low-frequency maps, such as the low Q regions in Eastern Tibetan plateau, Bohai Bay basin, and South Yellow Sea basin and the high Q areas in Northeast China Plate, south part of Huaihai basin, east part of the Dabieshan fold belts. The low-frequency band Q_{Lg} (0.2–1.0 Hz) has relatively lower Q than Q_0
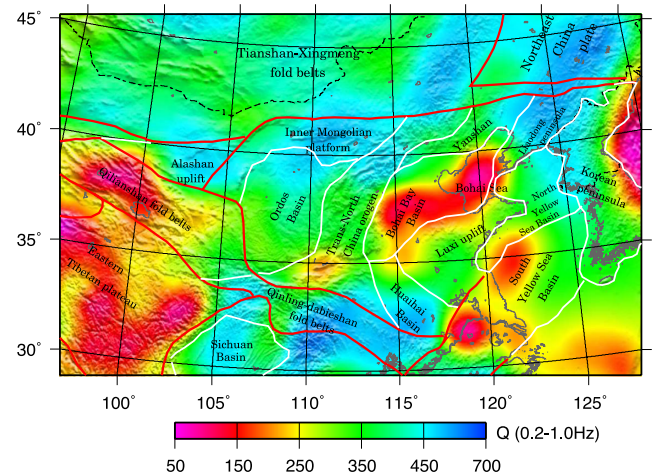
Figure 11. Map showing low-frequency band Q_{Lg} between 0.2 and 1.0 Hz. Note that the names of the geological blocks are labelled.

and display more smooth results than Q_0 map. Thus, similar to Q_0, the Q_{Lg} (0.2–1.0 Hz) may provide an additional robust definition for different geological blocks.

4.2 Crustal thickness and regional Q_{Lg}

Lg attenuation depends on both the geometrical parameters of the crust waveguide and its material properties (Zhang & Lay 1995; Wu *et al.* 2000). Zhao *et al.* (2010) investigated the
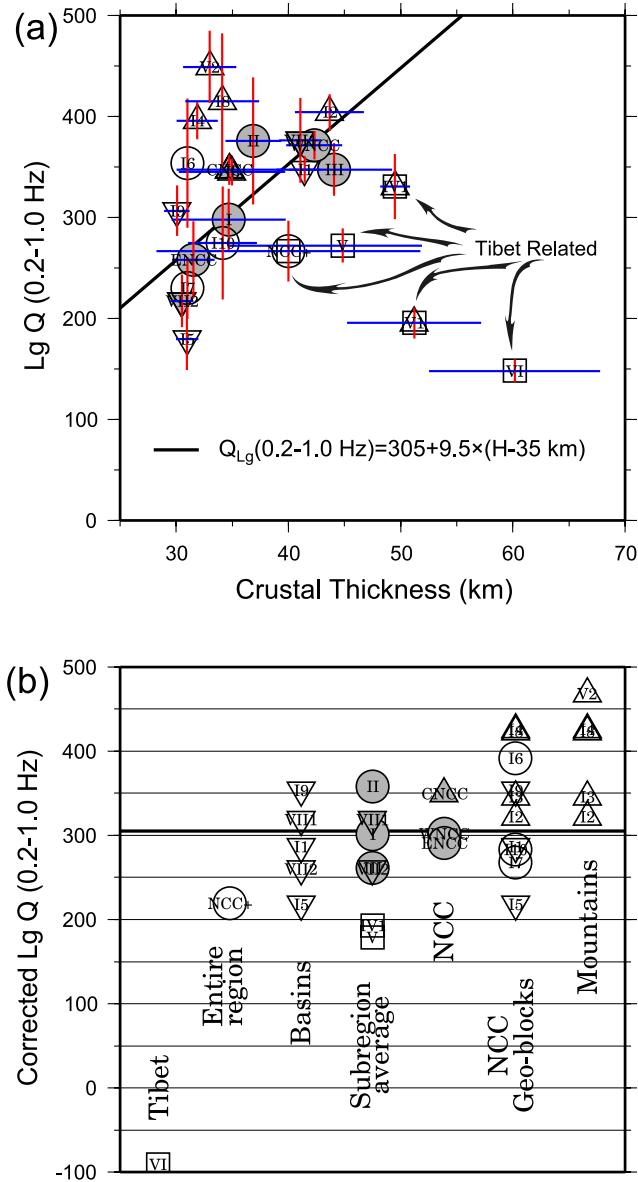
Figure 12. (a) Low-frequency Q_{Lg} (0.2–1.0 Hz) versus average crust thickness, where the red and blue segments are the error bars for Q_{Lg} and crustal thickness, respectively, the linear regressions is obtained from 8 subregional Q values (shaded symbols) excluding the Tibet related data. (b) Low-frequency Lg Q after corrected to 35-km-crustal thickness and grouped based on their geological features.

relationship between the low-frequency Q_{Lg} and the crust thickness in and around northeast China and found there appears to be positive correlation between the low-frequency Q_{Lg} (0.2–1.0 Hz) and crustal thickness, consistent with the empirical results by Zhang & Lay (1995). For the NCC and its vicinity, we find that there appears to be a similar relation except for eastern Tibetan plateau (VI), which is characterized by very thick crust but very low Q_{Lg}. Therefore, we use the major geological-blocks excluding the Eastern Tibetan plateau to investigate the relation between Q_{Lg} and crustal thickness. Fig. 12(a) shows the average low-frequency Q_{Lg} versus the average crustal thickness for various geological units in the NCC and its surrounding regions. These average Q_{Lg} values are calculated using the data in Fig. 11 between 0.2 and 1.0 Hz. The crustal thickness data are from the $2° \times 2°$ global crust model

CRUST2.0 (Bassin *et al.* 2000). The symbols in Fig. 12(a) denote different types of geological blocks and are explained in Table 1. The filled symbols are subregional averages excluding regions related to the Eastern Tibetan plateau. A linear relation between the Q_{Lg} and the crustal thickness, Q_{Lg} (0.2–1.0 Hz) $= 305 + 9.5 \times (H = 35$ km), is obtained by fitting these sub-regional averages and is shown as a solid line in Fig. 12(a), where H is the crust thickness. The blocks related to the Tibetan plateau are shown with squares and clearly disobey the Q_{Lg}-crust thickness relation. Using this relationship we corrected the observed average Q_{Lg} (0.2–1.0 Hz) to a reference crust thickness of 35 km and present the result in Fig. 12(b), where data points are grouped by geological context. The corrected average Q_{Lg} (0.2–1.0 Hz) is 219 for the entire investigated area, and 301 for the NCC. The low-frequency Q_{Lg} (0.2–1.0 Hz) in regions dominated by mountains (e.g. 350 for CNCC) appear to be higher than those dominated by basins (e.g. 291 and 302 for ENCC and WNCC). As evidenced in Fig. 12(b), the Q_{Lg} values from NCC blocks are scattered in a broad range, from 218 for the Bohai Bay basin (I_5) to 426 for the Yanshan range (I_4). The mountain areas has the highest Q_{Lg} (0.2–1.0 Hz), which is higher than the basin areas by approximately 100–150. However, there are still overlaps between basins and mountains.

4.3 Regional Q_{Lg} and heat flow

The regional variations of Lg attenuation can be attributed to many factors including thermal related activities in the crust and upper mantle. The thermal related activities can either be the cause or the result of geological activities. An investigation of the seismic wave attenuation may help to reveal the underlying thermal activities and to help understand present or past geological activities related to the evolution of the NCC. On the other hand, surface heat flow often is an indicator of subsurface thermal related activities. We examine the Lg attenuation and the heat flow data to check for any existing relationship between them.

We collect 265 surface heat-flow observations in and around the NCC (Wang & Huang 1990; Hu *et al.* 2000, 2001). Based on these heat flow data, the mean heat-flow values in individual geological blocks are calculated and listed in Table 1. We investigate the correlations between mean Q_{Lg} and mean heat-flow for different geological blocks at different frequency bands. Shown in Fig. 13 are mean surface heat flow values versus mean Q_{Lg}, together with their standard deviations. Although the data set is rather scattered, a negative correlation between mean Q_{Lg} and surface heat flow, $Heat\ flow = 73.604 - 0.034 \cdot Q_{Lg}$, can still be obtained. Because seismic attenuation observation can extend to broad surface area than the heat flow data, such a relationship may help to fill the insufficient heat flow coverage.

4.4 Lg-wave source spectra

During the joint inversion, we obtain the Lg-wave excitation functions at discrete frequencies. Fig. 14(a) illustrates source spectral functions for the event on July 25, 2006. The dots represent results for individual frequencies. With the ω^{-2} source model (Aki 1967; Brune 1970), we fit the Lg-wave excitation function to obtain the scalar seismic moment M_0 and the corner frequency f_c (Zhao *et al.* 2010). The solid line in Fig. 14(a) is the best-fitting source model for one event, and the shaded areas give their standard deviations. The inverted seismic moments and the corner frequencies for all 176 events are listed in Table S2.
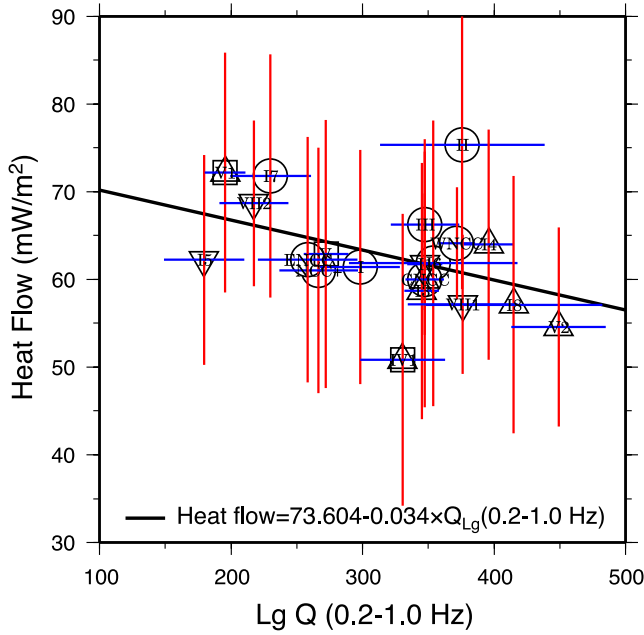
Figure 13. Heat flow data versus Q_{Lg} (0.2–2.0 Hz) for different geological blocks, where the red and blue segments are the error bars for heat flow and Q_{Lg}, respectively, and the solid line is obtained by using linear regressions.

Following Zhao *et al.* (2010), we apply linear regression to check the relations between M_0 and f_c under the assumption that either the stress drop is a constant or there is a theoretical exponent of -3 (Brune 1970), that is,

$$\log_{10}(M_0) = 15.19(\pm0.04) - 2.36(\pm0.11)\log_{10}(f_c), \qquad (8a)$$

$$\log_{10}(M_0) = 9.71 + \log_{10}(\Delta\sigma) - 3\log_{10}(f_c), \quad \Delta\sigma = 2.4\,\text{bar}, \qquad (8b)$$

where $\Delta\sigma$ is the stress drop in bar, and the M_0 is in Newton meters. The results are shown in Fig. 14(b), where the stress drops for those regional events are scattered between 0.1 and 50 bar, and a regional average, $\Delta\sigma = 2.49\,\text{bar}$, is plotted. Illustrated in Fig. 14(c) are the relationships between M_0 and the body-wave magnitude m_b reported by different regional seismic networks. A linear regression give the equation

$$\log_{10}(M_0) = 10.31(\pm0.28) + 0.93(\pm0.06)m_b, \quad SD = 0.54,$$

$$r = 0.74. \qquad (9a)$$

After we impose a unit slope, the equation become

$$\log_{10}(M_0) = 11.01(\pm0.27) + m_b, \quad SD = 0.52, \ r = 0.77, \quad (9b)$$

where the numbers in parentheses are standard errors, *SD* indicates the standard deviation and r denotes the correlation coefficient. In Fig. 14 the scaling rates tend to be self-similarity, being consistent with the previous results of Ide & Beroza (2001). These relations, observed in the NCC and its surrounding regions, are similar to our previous results obtained in Northeast China (Zhao *et al.* 2010).

5 DISCUSSION

In this study, a joint inversion method combining both dual- and single-station data is used for *Lg* attenuation tomography. The dual-station method is less affected by the unknown *Lg*-wave excita-
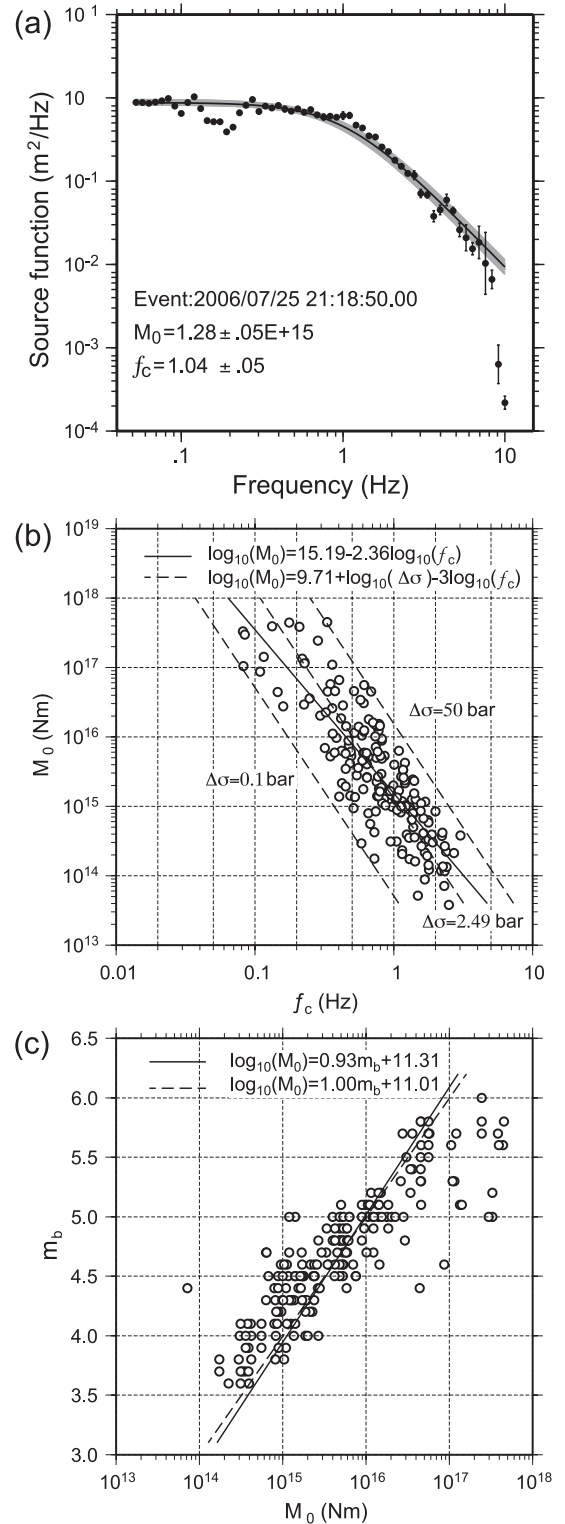
Figure 14. (a) Retrieved *Lg* excitation spectra for the regional earthquake on July 25, 2006. Dots are directly inverted results. Solid line is the best-fitting ω^{-2} source models, and shaded areas are their standard deviations. The resulted seismic moment M_0 and corner frequency f_c are labelled in the panel. (b) Seismic moment M_0 versus corner frequency f_c, where the solid line is the linear regression assuming a constant stress drop, while dashed lines are obtained based on the -3 scaling and variable stress drops. (c) Body-wave magnitude m_b versus seismic moment M_0, where the solid line is obtained using a linear regression and the dashed line is calculated using a unit slope, respectively.

tion function but usually has a lower spatial resolution because of limited interstation ray coverage. On the contrary, by using the event-station ray paths, the single-station method has better spatial resolution. However, the single-station method treats both source function and attenuation as unknowns for joint inversion, which may cause parameter trade-off between the attenuation and source functions (Menke *et al.* 2006; Xie 2006). Another issue is when the attenuation investigation is expanded into broadband, higher frequency information tends to be depleted within a short distance. This is particularly important when investigating high-frequency attenuation in strongly attenuated regions such as the Tibetan plateau. Under this circumstance, the data from short-distance stations are crucial, while the dual-station data are usually from farther stations than those used by the single-station method. Given these considerations, we first use the dual-station method to generate a low resolution Q_{Lg} model at each frequency. Then, using this as the initial model, we combine both the dual- and single-station data together to jointly invert the attenuation and Lg excitation functions. Based on this strategy, the Lg Q tomography can improve tomographic resolution, especially for high frequencies. To a certain extent and within a studied regional network, this scheme can reduce some potential errors caused by the cross talk between the attenuation and source terms.

In our broad-band Q_{Lg} model (see Figs 9 and 10), high Q_{Lg} values correspond to the relatively stable regions in the west and central NCC, while low Q_{Lg} values arise in the Bohai Bay basin, the South Yellow Sea basin, and the Eastern Tibetan plateau. Using numerical simulations, Zhang & Lay (1995), Shapiro *et al.* (1996) and Wu *et al.* (2000) demonstrated that heterogeneities of different scales can strongly attenuate Lg-wave propagation in crustal waveguide. Near-surface sedimentary layers and the water column are known to significantly contribute to increased attenuation (Cao & Muirhead 1993; Shapiro *et al.* 1996; Ottemöller 2002). The Indo-Eurasian collision created the Tibetan plateau, where exists a vastly thickened crust, a doublet Moho structure, inferred high temperature and low-viscosity channel flows (e.g. Francheteau *et al.* 1984; Nelson *et al.* 1996; Li *et al.* 2011). The plateau was found to be characterized by unusually low Q_{Lg} by previous investigators (Fan & Lay 2003a,b; Xie *et al.* 2004). In this study, we find that the Eastern Tibetan plateau has the lowest Q_{Lg} values among all geology units (Fig. 12b). The attenuation in the Tibetan plateau and its surrounding regions is apparently biased from the Q_{Lg}-crust thickness relation (Fig. 12a). This suggests that the Lg attenuation mechanism could be distinctive within the Tibetan crust. Therefore, the attenuation-crustal thickness relation is obtained excluding the Tibetan plateau and its surrounding regions. On the other hand, the link between Lg attenuation and characteristics such as a double-layer curst and underlying thermal activities may suggest the Lg attenuation could be a useful tool for investigating the evolution of the Tibetan plateau.

6 CONCLUSIONS

Based on the broad-band Lg-wave data, we obtain a tomographic Q_{Lg} model for the NCC and its surrounding regions. The inversions are independently conducted at individual frequencies. There is no *a priori* constraint on the frequency dependence of the Q_{Lg} model or source spectra applied to the inversion. Limited by the available data, frequency-dependent site responses and source radiation patterns are not considered in our inversion.

We use the conventional Lg group-velocity window of 3.6–3.0 km s^{-1} to calculate the Lg-wave spectra for all frequencies. Although the Rayleigh wave could be involved in this window in a low frequency band, that is, between 0.05 and 0.5 Hz, we treat the windowed wave train as Lg phase only. Both Lg-wave amplitudes and noise levels vary within the frequency band, causing different signal-to-noise ratios at individual frequencies. We use a pre-P-wave time window to calculate the noise spectra, which is used to correct the Lg spectra (Ringdal *et al.* 1992; Schlittenhardt 2001). These may introduce errors because the noise spectrum is time varying. The unevenly distributed sources and stations make the ray coverage change geographically. The checkerboard testing method is used to investigate the inversion resolution. The best data coverage is in the NCC and between frequencies 0.05 and 2.0 Hz, where the Q_{Lg} model has the highest resolution of approximately 1° × 1°. Towards higher frequencies and in the surrounding regions, the resolution deteriorated.

In the NCC, Q_0 has an average value of 374 and an increasing trend from east to west, with average values of 337, 361 and 421 for the east, central and west blocks. For the surrounding regions, the Eastern Tibetan plateau has a very low Lg Q_0 of 188, while both the Northeast China Plate and the Tianshan-Xingmeng fold belts are characterized by high Q_0 values of 506 and 424, respectively. An apparent Q_0 difference of about 210 is observed between the western Qilianshan fold belts and the eastern Qinling-Dabieshan fold belts. The Q_0 values correlate well with the local tectonics, but show apparent difference between the east and west NCC, such as the basins between east and west.

Using the statistical method, we investigate the Q_{Lg} frequency dependence both for the entire region and for subregions such as the basin and mountain areas. Within the investigated area, the Q_{Lg} values show large regional variations at lower frequencies (0.2–1.0 Hz) than at higher frequencies (above 2.0 Hz) (refer to Fig. 12). However, in some areas, the high-frequency attenuation appears to be related to some very local features such as very rough terrains. Their relationship will need additional investigation. Zhao *et al.* (2010) obtained a weak correlation between the low-frequency Q_{Lg} and the crustal thickness in Northeast China. A similar relationship can be found in and around the NCC. We use this relationship to correct the effects of the crustal thickness on Q_{Lg}, and group the results from different geological units. The results show systematic differences among different geological units. For example, the mean values of the crust-thickness corrected Q_{Lg} were about 270 and 390 for the basin and mountain groups, although certain overlaps are seen between the western basins and eastern mountains (see Fig. 12b). Using a similar statistical method, we also investigate the relationship between the attenuation and the surface heat flow. Although there are large scatters in the data, the mean crust-thickness corrected Q_{Lg} is inversely correlated to the mean heat flow.

The inverted Lg-wave excitation spectra can be reasonably fit by a ω^{-2} source model (Aki 1967; Brune 1970), which gives the seismic moment M_0 and the corner frequency f_c. A linear relation with a slope of -2.36 is obtained between $\log_{10}(M_0)$ and $\log_{10}(f_c)$. This slope is close to the theoretical prediction of -3 by Brune (1970). Comparing $\log_{10}(M_0)$ with the body-wave magnitudes reported by the regional networks, we obtain a linear scaling relation with a slope of 0.93. The relationships are consistent with the previous results and thus provide an additional support for our Lg attenuation model.

REFERENCES

Aki, K., 1967. Scaling law of seismic spectrum, *J. geophys. Res.,* **72,** 729–740.

Al-Damegh, K., Sandvol, E., Al-Lazki, A. & Barazangi, M., 2004. Regional seismic wave propagation (Lg and Sn) and Pn attenuation in the Arabian Plate and surrounding regions, *Geophys. J. Int.,* **157,** 775–795.

An, M.J. & Shi, Y.L., 2006. Lithospheric thickness of the Chinese continent, *Phys. Earth planet. Inter.,* **159,** 257–266.

Bao, X.Y., Sandvol, E., Ni, J., Hearn, T., Chen, Y.S.J. & Shen, Y., 2011. High resolution regional seismic attenuation tomography in eastern Tibetan Plateau and adjacent regions, *Geophys. Res. Lett.,* **38,** L16304, doi:10.1029/2011GL048012.

Bassin, C., Laske, G. & Maters, G., 2000. The current limits of resolution for surface wave tomography in North America, *EOS, Trans. Am. geogphys. Un.,* **81,** F897.

Benz, H., Frankel, A. & Boore, D., 1997. Regional Lg attenuation for the continental United States, *Bull. seism. Soc. Am.,* **87,** 606–619.

Bird, P., 1979. Continental delamination and the Colorado Plateau, *J. geophys. Res.,* **84,** 7561–7571.

Bouchon, M., 1982. The complete synthesis of seismic crustal phases at regional distances, *J. geophys. Res.,* **87,** 1735–1741.

Boyd, F.R., 1989. Compositional distinction between oceanic and cratonic lithosphere, *Earth planet. Sci. Lett.,* **96,** 15–26.

Brune, J.N., 1970. Tectonic stress and the spectra of seismic shear waves from earthquakes, *J. geophys. Res.,* **75,** 4997–5009.

Campillo, M., 1987. Lg wave propagation in a laterally varying crust and the distribution of the apparent quality factor in central France, *J. geophys. Res.,* **92,** 12 604–12 614.

Campillo, M., Feignier, B.M., Bouchon, M. & Béthoux, N., 1993. Attenuation of crustal waves across the Alpine range, *J. geophys. Res.,* **98,** 1987–1996.

Cao, A. & Muirhead, K.J., 1993. Finite difference modelling of Lg blockage, *Geophys. J. Int.,* **115,** 85–96.

Chen, J.F., Xie, Z., Li, H.M., Zhang, X.D., Zhou, T.X., Park, Y.S., Chen, D.G. & Zhang, X., 2003. U-Pb zircon ages for a collision-related K-rich complex at Shidao in the Sulu ultrahigh pressure terrane, *China Geochem. J.,* **37,** 35–46.

Chen, L. & Ai, Y., 2009. Discontinuity structure of the mantle transition zone beneath the North China Craton from receiver function migration, *J. geophys. Res.,* **114,** B06307, doi:10.1029/2008JB006221.

Chen, L., Zheng, T.Y. & Xu, W.W., 2006. A thinned lithospheric image of the Tanlu Fault Zone, Northeastern China: constructed from wave equation based receiver function migration, *J. geophys. Res.,* **111,** B09312, doi:10.1029/2005JB003974.

Chun, K.-Y., West, G.F., Kokoski, R.J. & Samson, C., 1987. A novel technique for measuring Lg attenuation results from eastern Canada between 1 to 10 Hz, *Bull. seism. Soc. Am.,* **77,** 398–419.

Cong, L., Hu, J., Fu, Z., Wen, Y., Kang, G. & Wu, X., 2002. Lg coda Q distribution in China continental area and its adjacent regions, *Sci. China (Ser. D),* **32,** 617–625.

Deng, J.F., Su, S.G., Niu, Y.L., Liu, C., Zhao, G.C., Zhao, X.G., Zhou, S. & Zhou, Z.X., 2007. A possible model for the lithospheric thinning of North China craton: evidence from the Yanshanian (Jura-Cretaceous) magmatism and tectonism, *Lithos,* **96,** 22–35.

Doin, M.P., Fleitout, L. & Christensen, U., 1997. Mantle convection and stability of depleted and undepleted continental lithosphere, *J. geophys. Res.,* **102,** 2771–2787.

Fan, G.W. & Lay, T., 2002. Characteristics of Lg attenuation in the Tibetan Plateau, *J. geophys. Res.,* **107**(B10), 2256, doi:10.1029/2001JB000804.

Fan, G.W. & Lay, T., 2003a. Strong Lg wave attenuation in the Northern and Eastern Tibetan Plateau measured by a two-station/two-event stacking method, *Geophys. Res. Lett.,* **30**(10), 1530, doi:10.1029/2002GL016211.

Fan, G.W. & Lay, T., 2003b. Strong Lg attenuation in Tibetan Plateau, *Bull. seism. Soc. Am.,* **93,** 2264–2272.

Ford, S.R., Dreger, D.S., Mayeda, K., Walter, W.R., Malagnini, L. & Phillips, W.S., 2008. Regional Attenuation in Northern California: a comparison of five 1D Q methods, *Bull. seism. Soc. Am.,* **98,** 2033–2046.

Francheteau, J., Jaupart, C., Shen, X.J., Kang, W.H., Lee, D.L., Bai, J.C., Wei, H.P. & Deng, H.Y., 1984. High heat-flow in Southern Tibet, *Nature,* **307,** 32–36.

Gao, S. *et al.*, 2004. Recycling lower continental crust in the North China craton, *Nature,* **432,** 892–897.

Ge, H., Ni, Y., Huang, C., Li, J., Li, Y., Jiang, Y. & Lu, F., 1989. Lg velocity, attenuation and magnitude of the continent area in China (in Chinese), *Chin. Sci. Bull.,* **24,** 1889–1892.

Griffin, W.L., Andi, Z., O'Reilly, S.Y. & Ryan, C.J., 1998. Phanerozoic evolution of the lithosphere beneath the Sino-Korean craton, in *Mantle Dynamics and Plate Interactions in East Asia,* Geodyn. Ser., Vol. 27, pp. 107–126, eds Flower, M., Chung, S.L., Lo, C.H. & Lee, T.Y., American Geophysical Union, Washington, DC.

Hao, T.Y., Mancheol, S., Liu, J., Yan, X., Suckwon, C., Liu, S., Dai, M. & Xu, Y., 2004. Deep structure and boundary belt position between Sino-Korean and Yangzi blocks in Yellow Sea (in Chinese with English abstract), *Earth Sci. Front.,* **11,** 51–61.

Hearn, T.M., Wang, S., Pei, S., Xu, Z., Ni, J.F. & Yu, Y., 2008. Seismic amplitude tomography for crustal attenuation beneath China, *Geophys. J. Int.,* **174,** 223–234.

Herrin, E. & Richmond, J., 1960. On the propagation of the Lg phase, *Bull. seism. Soc. Am.,* **50,** 197–210.

Hong, T.K., 2010. Lg attenuation in a region with both continental and oceanic environments, *Bull. seism. Soc. Am.,* **100,** 851–858.

Houseman, G.A., McKenzie, D.P. & Molnar, P., 1981. Convective instability of a thickened boundary layer and its relevance for the thermal evolution of continental convergent belts, *J. geophys. Res.,* **86**(B7), 6155–6132.

Hu, S., He, L. & Wang, J.-Y., 2000. Heat flow in the continental area of China: a new data set, *Earth planet. Sci. Lett.,* **179,** 407–419.

Hu, S., He, L. & Wang, J.-Y., 2001. Compilation of heat flow data in the China continental area (3rd edn), *Chin. J. Geophys.,* **44,** 611–626.

Huang, Z., Su, W., Peng, Y., Zheng, Y. & Li, H., 2003. Rayleigh wave tomography of China and adjacent regions, *J. geophys. Res.,* **108**(B2), 2073, doi:10.1029/2001JB001696.

Ide, S. & Beroza, G.C., 2001. Does apparent stress vary with earthquake size? *Geophys. Res. Lett.,* **28,** 3349–3352.

Ji, S.C., Wang, Q., Marcotte, D., Salisbury, M.H. & Xu, Z.Q., 2007. P-wave velocities, anisotropy and hysteresis in ultrahigh-pressure metamorphic rocks as a function of confining pressure, *J. geophys. Res.,* **112,** B09204, doi:10.1029/2006JB004867.

Jin, A. & Aki, K., 1988. Spatial and temporal correlation between coda Q and seismicity in China, *Bull. seism. Soc. Am.,* **78,** 741–769.

Jun, P.R., Gap, K.H. & Pu, J.G., 1996. *Geology of Korea,* Foreign languages books publishing house, Pyongyang, 382 pp.

Kennett, B.L. N., 1986. Lg waves and structural boundaries, *Bull. seism. Soc. Am.,* **76,** 1133–1141.

Knopoff, L., Schwab, F. & Kausel, E., 1973. Interpretation of Lg, *Geophys. J. R. astr. Soc.,* **33,** 389–404.

Li, X., Wei, D., Yuan, X., Kind, R., Kumar, P. & Zhou, H., 2011. Details of the Doublet Moho Structure beneath Lhasa, Tibet, Obtained by Comparison of P and S Receiver Functions, *Bull. seism. Soc. Am.,* **101,** 1259–1269.

Lu, F.-X., Zheng, J., Shao, J., Zhang, R., Chen, M. & Cheng, Z., 2006. Asthenospheric upwelling and lithospheric thinning in late Cretaceous-Cenozoic in eastern North China, *Earth Sci. Front.,* **13,** 86–92.

Ma, X.Y., Ding, G.Y., Gao, W.X., Zhang, H.G., Zhang, B.C. & Ma, Z.J., 1989. *Lithospheric Dynamics Atlas of China,* China Cartographic Publishing House, Beijing, 4 pp.

Menke, W., Holmes, R.C. & Xie, J., 2006. On the nonuniqueness of the coupled origin time-velocity tomography problem, *Bull. seism. Soc. Am.,* **96,** 1131–1139.

Menzies, M.A. & Xu, Y.G., 1998. Geodynamics of the North China Craton, in *Mantle Dynamics and Plate Interactions in East Asia,* Geodyn. Ser., Vol. 27, pp. 155–165, eds Flower, M., Chung, S.-L., Lo, C.-H. & Lee, T.-Y., American Geophysical Union, Washington, DC.

Menzies, M.A., Xu, Y.G., Zhang, H.F. & Fan, W.M., 2007. Integration of geology, geophysics and geochemistry: a key to understanding the North China Craton, *Lithos, ***96,** 1–21.

Menzies, M.A., Fan, W.M. & Zhang, M., 1993. Palaeozoic and Cenozoic lithoprobes and the loss of >120 km of Archaean lithosphere, Sino-Korean craton, China, in *Magmatic Processes and Plate Tectonics,* Vol. 76, pp. 71–81, eds Prichard, H.M., Alabaster, T., Harris, N.B.W. & Neary, C.R., Geol. Soc. Spcl. Pub.

Mitchell, B.J., 1995. Anelastic structure and evolution of the continental crust and upper mantle from seismic surface wave attenuation, *Rev. Geophys.,* **33,** 441–462.

Mitchell, B.J., Cong, L. & Ekström, G., 2008. A continent-wide map of 1-Hz Lg coda Q variation across Eurasia and its relation to lithospheric evolution, *J. geophys. Res.,* **113,** B04303, doi:10.1029/2007JB005065.

Mitchell, B.J., Pan, Y., Xie, J. & Cong, L., 1997. Lg coda Q variation across Eurasia and its relation to crustal evolution, *J. geophys. Res.,* **102,** 22 767–22 780.

Morgan, J.S., Christeson, G.L. & Zelt, C.A., 2002. Testing the resolution of a 3D velocity tomogram across the Chicxulub crater, *Techonophysics,* **355,** 215–226.

Morozov, I.B., 2010. Attenuation coefficients of Rayleigh and Lg waves, *J. seism.,* **14,** 803–822.

Nelson, K.D. *et al.*, 1996. Partially molten middle crust beneath southern Tibet: synthesis of project INDEPTH results, *Science,* **274,** 1684–1688.

Ottemöller, L., 2002. Lg wave Q tomography in Central America, *Geophys. J. Int.,* **150,** 295–302.

Ottemöller, L., Shapiro, N.M., Singh, S.K. & Pacheco, J.F., 2002. Lateral variation of Lg wave propagation in southern Mexico, *J. geophys. Res.,* **107,** doi:10.1029/2001JB000206.

Owens, T.J. & Zandt, G., 1997. Implications of crustal property variations for models of Tibetan plateau evolution, *Nature,* **387,** 37–43.

Paige, C.C. & Saunders, M.A., 1982. LSQR: An algorithm for sparse linear equations and sparse least squares, *ACM Trans. Math. Softw.,* **8,** 43–71.

Panza, G.F. & Calcagnile, G., 1975. Lg, Li and Rg from Rayleigh modes, *Geophys. J. R. astr. Soc.,* **40,** 475–487.

Pasyanos, M.E., Matzel, E.M., Walter, W.R. & Rodgers, A.J., 2009. Broadband Lg attenuation modelling in the Middle East, *Geophys. J. Int.,* **177,** 1166–1176.

Pei, S., Zhao, J., Rowe, C.A., Wang, S., Hearn, T.M., Xu, Z., Liu, H. & Sun, Y., 2006. M_L amplitude tomography in north China, *Bull. seism. Soc. Am.,* **96,** 1560–1566.

Phillips, W.S., Hartse, H.E. & Rutledge, J.T., 2005. Amplitude ratio tomography for regional phases Q, *Geophys. Res. Lett.,* **32,** L21301, doi:10.1029/2005GL023870.

Phillips, W.S., Hartse, H.E. & Taylor, S.R., 2000. 1Hz Lg Q tomography in central Asia, *Geophys. Res. Lett.,* **20,** 3425–3428.

Ringdal, F., Marshall, P.D. & Alewine, R.W., 1992. Seismic yield determination of Soviet underground explosions at the Shagan River test site, *Geophys. J. Int.,* **109,** 65–77.

Rodgers, A.J. & Schwartz, S.Y., 1998. Lithospheric structure of the Qiangtang terrane, northern Tibetan plateau, from complete regional waveform modeling: evidence for partial melt, *J. geophys. Res.,* **103,** 7137–7152.

Rudnick, R.L. & Niblade, A.A., 1999. The thickness and heat production of Archean lithosphere: constraints from xenolith thermo barometry and surface heat flow, in *Mantle Petrology: Field Observations and High Pressure Experimentation,* Vol. **6,** pp. 3–12, eds Fei, Y., Bertika, C.M. & Mysen, B.O., The Geochemical Society, Special Publications.

Santosh, M., Tsunogae, T., Ohyama, H., Sato, K., Li, J.H. & Liu, S.J., 2008. Carbonic metamorphism at ultrahigh-temperatures: evidence from North China Craton, *Earth planet. Sci. Lett.,* **266,** 149–165.

Schlittenhardt, J., 2001. Teleseismic Lg of Semipalatinsk and Novaya Zemlya nuclear explosions recorded at the GRF (Gräfenberg) array: comparison with regional Lg (BRV) and their potential for accurate yield estimation, *Pure appl. Geophys.,* **158,** 2253–2274.

Shapiro, N., Béthous, N., Campillo, M. & Paul, A., 1996. Regional seismic phases across the Ligurian sea: Lg blockage and oceanic propagation, *Phys. Earth plant. Inter.,* **93,** 257–268.

Shen, X., Zhou, H. & Kawakatsu, H., 2008. Mapping the upper mantle discontinuities beneath China with teleseismic receiver functions, *Earth Planets Space,* **60,** 713–719.

Street, R.L., Herrmann, R.B. & Nuttli, O.W., 1975. Spectral characteristics of the Lg wave generated by central United States earthquakes, *Geophys. J. R. astr, Soc,* **41,** 51–63.

Su, W., Wu, J., Ming, L. & Wang, C., 2006. Lg coda Q_0 value and its relation with the tectonics in Chinese mainland and adjacent regions, *Acta Seismol. Sin.,* **28,** 133–140.

Turner, S. *et al.*, 1996. Post-collision, shoshonitic volcanism on the Tibetan Plateau: implications for convective thinning of the lithosphere and the source of ocean island basalts, *J. Petrol.,* **37,** 45–71.

Wang, J.-Y. & Huang, S.-P., 1990. Compilation of heat flow data in the China continental area (2nd edn.) (in both Chinese and English), *Seism. Geol.,* **12,** 351–366.

Wessel, P. & Smith, W., 1998. New, improved version of the generic mapping tools released, *EOS, Trans. Am. Geophys. Un.,* **79,** 579.

Wu, F., Yang, J., Zhang, Y. & Liu, X., 2006. Emplacement ages of the Mesozoic granites in southeastern part of the Western Liaoning Province, *Acta Petrol. Sin.,* **22,** 315–325.

Wu, F.Y., Lin, J.Q., Wilde, S.A., Zhang, X.O. & Yang, J.H., 2005. Nature and significance of the Early Cretaceous giant igneous event in eastern China, *Earth planet. Sci. Lett.,* **233,** 103–119.

Wu, R.-S., Jin, S. & Xie, X.-B., 2000. Energy partition and attenuation of Lg waves by numerical simulations using screen propagators, *Phys. Earth planet. Inter.,* **120,** 227–244.

Xie, J., 2002. Lg Q in the eastern Tibetan Plateau, *Bull. seism. Soc. Am.,* **92,** 871–876.

Xie, J., 2006. Fundamental limitations in resolving power of Q tomography, *Seism. Res. Lett.,* **77,** 197.

Xie, J., 1993. Simultaneous inversion for source spectrum and path-Q using Lg with application to 3 Semipalatinsk explosions, *Bull. seism. Soc. Am.,* **83**(5), 1547–1562.

Xie, J., Gok, R., Ni, J. & Aoki, Y., 2004. Lateral variations of crustal seismic attenuation along the INDEPTH profiles in Tibet from Lg Q inversion, *J. geophys. Res.,* **109,** B10308, doi:10.1029/2004JB002988.

Xie, J., Wu, Z., Liu, R., Schaff, D., Liu, Y. & Liang, J., 2006. Tomographic regionalization of crustal Lg Q in eastern Eurasia, *Geophys. Res. Lett.,* **33,** L03315, doi:10.1029/2005GL024410.

Xie, X.B. & Lay, T., 1994. The excitation of Lg waves by explosions: a finite-difference investigation, *Bull. seism. Soc. Am.,* **84,** 324–342.

Xu, Y.-G., 2001. Thermo-tectonic destruction of the Archaean lithospheric keel beneath the Sino-Korean Craton in China: evidence, timing and mechanism, *Phys. Chem. Earth (A),* **26,** 747–757.

Xu, Y.-G., 2007. Diachronous lithospheric thinning of the North China craton and formation of the Daxin'anling-Taihangshan gravity lineament, *Lithos,* **96,** 281–298.

Zelt, C., 1998. Lateral velocity resolution from three-dimensional seismic refraction data, *Geophys. J. Int.,* **135,** 1101–1102.

Zhang, T.R. & Lay, T., 1995. Why the Lg phase does not traverse oceanic crust, *Bull seism. Soc. Am.,* **85,** 1665–1678.

Zhao, D.P., 2004. Global tomographic mages of mantle plumes and subducting slabs: insight into deep earth dynamics, *Phys. Earth plant. Inter.,* **146,** 3–24.

Zhao, G.C., Sun, M. & Wilde, S.A., 2003. Correlations between the eastern block of the North China Craton and the South Indian block of the Indian

shield: an Archaean to Palaeoproterozoic link, *Precamb. Res.,* **122,** 201–233.

Zhao, G.C., Wilde, S.A., Cawood, P.A. & Sun, M., 2001. Archean blocks and their boundaries in the North China Craton: lithological, geochemical, structural and *P–T* path constraints and tectonic evolution, *Precamb. Res.,* **107,** 45–73.

Zhao, L. & Zheng, T., 2007. Complex upper-mantle deformation beneath the North China Craton: implications for lithospheric thinning, *Geophys. J. Int.,* **170,** 1095–1099

Zhao, L.-F., Xie, X.-B., Wang, W.-M., Zhang, J.-H. & Yao, Z.-X., 2010. Seismic Lg-wave Q tomography in and around Northeast China, *J. geophys. Res.,* **115,** B08307, doi:10.1029/2009JB007157.

Zhao, L.-F., Xie, X.-B., Wang, W.-M. & Yao, Z.-X., 2008. Regional seismic characteristics of the 9 October 2006 North Korean nuclear test, *Bull. seism. Soc. Am.,* **98,** 2571–2589.

Zheng, X.F., Yao, Z.X., Liang, J.H. & Zheng, J., 2010. The role played and opportunities provided by IGP DMC of China National Seismic Network in Wenchuan earthquake disaster relief and researches, *Bull. seism. Soc. Am.,* **100,** 2866–2872.

Zor, E., Sandvol, E., Xie, J., Türkelli, N., Mitchell, B., Gasanov, A.H. & Yetirmishli, G., 2007. Crustal attenuation within the Turkish plateau and surrounding regions, *Bull. seism. Soc. Am.,* **97,** 151–161.

SUPPORTING INFORMATION

Additional Supporting Information may be found in the online version of this article:

Table S1. The station parameters used in this study.
Table S2. The event parameters used in this study (http://gji. oxfordjournals.org/lookup/supp1/doi:10.1093/gji/ggt235/-/DC1).

Please note: Oxford University Press is not responsible for the content or functionality of any supporting materials supplied by the authors. Any queries (other than missing material) should be directed to the corresponding author for the article.